AN ABSTRACT OF THE THESIS OF

Michael Prier for the degree of Master of Science in Mechanical Engineering presented on December 6, 2018.

Title: Energy Harvesting Performance of a Flapping Foil with Leading Edge Motion.

Abstract approved:

_____

James Liburdy

Force data for a flapping foil energy harvester with active leading edge motion operating in the low reduced frequency range is collected to determine how leading edge motion affects energy harvesting performance. The foil pivots about the mid-chord and operates in the low reduced frequency range of $fc/U_\infty = 0.06$, 0.08, and 0.10 with $Re = 20{,}000 - 30{,}000$, with a pitching amplitude of $\theta_0 = 70°$, and a heaving amplitude of $h_0 = 0.5c$. It is found that leading edge motions that reduce the effective angle of attack early the stroke work to both increase the lift forces as well as shift the peak lift force later in the flapping stroke. Leading edge motions in which the effective angle of attack is increased early in the stroke show decreased performance. In addition a discrete vortex model with vortex shedding at the leading edge is implement for the motions studied; it is found that the mechanism for shedding at the leading edge is not adequate for this parameter range and the model consistently over predicts the aerodynamic forces.

Energy Harvesting Performance of a Flapping Foil with Leading Edge Motion

by
Michael Prier

A THESIS

submitted to

Oregon State University

in partial fulfillment of
the requirements for the
degree of

Master of Science

Presented December 6, 2018
Commencement June 2019

Master of Science thesis of Michael Prier presented on December 6, 2018

APPROVED:

Major Professor, representing Mechanical Engineering

Head of the School of Mechanical, Industrial, and Manufacturing Engineering

Dean of the Graduate School

I understand that my thesis will become part of the permanent collection of Oregon State University libraries. My signature below authorizes release of my thesis to any reader upon request.

Michael Prier, Author

ACKNOWLEDGEMENTS

The author expresses sincere appreciation to Dr. James Liburdy for providing the opportunity and resources to study the problems presented here. His patience, guidance, and enthusiasm were essential for the success of this work.

In addition, I would like to thank my committee members Dr. Sourabh Apte, Dr. Joshua Gess, and Dr. Rakesh Gupta for their time and feedback.

I would like to thank my labmates Firas Siala, Forrest Anderson, Brian Tost, Reza Ziazi, and Ivan Nepomnyashchikh for their encouragement and insightful discussion.

Finally I would like to thank my family for their support and encouragement.

TABLE OF CONTENTS

TABLE OF CONTENTS (Continued)

LIST OF FIGURES

LIST OF FIGURES (Continued)

LIST OF FIGURES (Continued)

LIST OF FIGURES (Continued)

1 Introduction

The burning of fossil fuels has contributed to a warming climate over the last century resulting in the death of wild life and enhancing natural disasters such as hurricanes and drought. In response there has been a drive to explore and develop alternative and renewable energy sources such as wind and solar power. The first of these while successful is not without drawbacks; traditional spinning turbines have high tip speeds which are detrimental to wildlife while also inducing large mechanical stresses in the turbine itself decreasing the lifespan of the blade and increasing the cost of manufacturing. The cross sectional area swept by the turbine is circular making traditional turbine arrays less economical in flow area with space restrictions such as shallow riverbeds where multiple smaller turbines would be needed to span the flow area.

Flapping foil energy harvesters seek to improve upon their conventional spinning counter parts by eliminating the deficiencies listed above. Flapping foil energy harvesters are a dynamic system typically consists of a foil that is allowed to rotate about a set point along the chord length and translate perpendicular to the flow. The rotation of the wing, known as pitch, changes the angle of attack in the flow thereby generating a force that moves the foil in its translational degree of freedom known as heave; these mechanisms are shown in Figure 1.1. These novel energy harvesters have much lower tip speeds then rotating turbines and can be designed to sweep a particular cross section of flow by varying the amplitude of translation and the span of the foil.

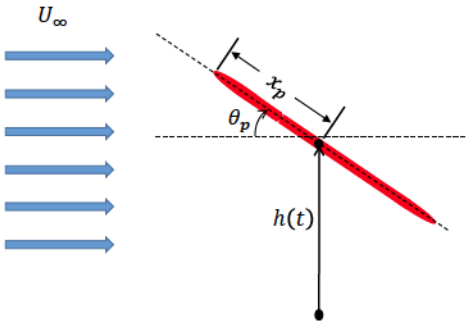

FIGURE 1.1: Flapping foil with rotational motion θ and translational motion h in a freestream U_∞

Unlike conventional turbines, flapping foils are unsteady and exhibit a phenomenon known as dynamic stall. Dynamic stall occurs when a vortex structure named a leading edge vortex (LEV) forms do to flow separation at the leading edge of the airfoil. As the angle of attack is increased during the motion, an adverse pressure gradient originates at the trailing edge and travels up the chord toward the leading edge where it causes flow separation and the formation of the LEV. An illustration of this process is shown in Figure 1.2. The LEV creates a low pressure region and when near the surface of the foil provides significant lift augmentation. The LEV suppresses loss of lift typical of stall scenarios until it convects away from the foil. These unsteady flow physics have preoccupied much of the research on both flapping foil energy harvesters and flapping foil flight.

Experimental flapping foil devices are restricted to three generic configurations. The first type are fully activated systems in which both pitch and heave motion profiles are forced regardless of the flow scenario. These devices do not harvest energy but are useful for investigating how different foil kinematics create different flow regimes. From this the fundamental physics of the problem can be investigated via force measurements from load cells or flow visualization such as PIV.

A second device category is semi-activated systems in which the pitch motion is forced and the foil is allowed to heave from the forces generated by the interaction of the foil

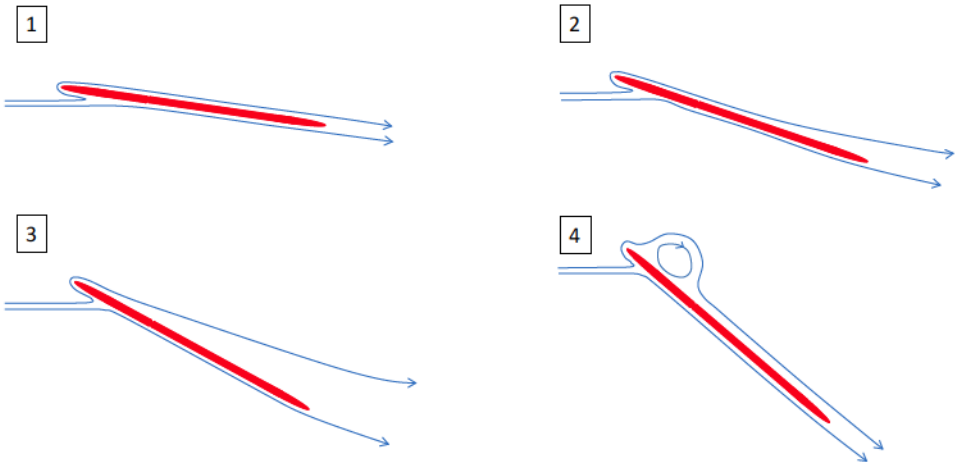

FIGURE 1.2: Process of dynamic stall. (1) Foil is at low angle of attack and flow is attached over entire chord length. (2) Angle of attack increases and an adverse pressure gradient develops on the trailing edge. (3) Angle of attack increases further and adverse pressure gradient travels up towards leading edge. (4) Adverse pressure gradient reaches the leading edge initiating LEV formation.

and the fluid. The pitching motion can be thought of as a driving mechanism for the heaving motion. These devices do extract energy from the flow and are feasible for real world applications.

Finally fully passive systems require no forced motion of the foil and involve either a mechanical mechanism to create the sinusoidal pitch such as a rotational spring, or mechanical coupling of the pitch and heave mechanisms. These devices are desirable because they require no active input to sustain their motion.

Because the LEV originates from the leading edge, it is anticipated that relative motion of the leading edge has the potential to affect the energy harvesting performance of flapping foils. While a limited number of studies have looked at leading edge motion, the parameter spaces is largely unexplored. It has been shown that passive flexibility at the leading edge is largely ineffective at increasing energy harvesting performance while certain active control mechanisms can be beneficial. However, studies looking at a wide range of leading edge motions are largely absent.

The focus of the following research is twofold. First experiments measuring aerodynamic forces on a pitching and heaving airfoil with controlled leading edge motion are conducted to determined how the phase of leading edge motion impacts energy harvesting performance. In addition to experimental force measurements, an inviscid model with a criteria for vortex shedding at the leading edge will be applied to the foil motions. This model has been shown to accurately predict forces for flow scenarios in which the flow is attached at the trailing edge. Here the model is applied to a parameter range in which flow separation at the trailing edge is anticipated and the foil geometry changes in time. Therefore, the second focus of this work is to determine whether the vortex shedding mechanism used here is appropriate for this parameter range, and how accurately the model is able to reproduce the experimental forces.

2 Background

2.1 Foil Motion

As seen in Figure 1.1, the motion of the airfoil consists of a sinusoidal pitch θ_p and heave motion h with the pitch leading the heave by 90° and the beginning of the cycle is the start of the downstroke:

$$\theta_p = -\theta_0 \sin(\omega t) \tag{2.1}$$

$$h = h_0 \cos(\omega t) \tag{2.2}$$

where $\omega = 2\pi f$ is the angular frequency and f is the heave and pitch frequency. The time derivative of these quantities is denoted with the overhead dot $\dot{\theta}_p, \dot{h}$ respectively. Positive pitch is considered clock-wise. The foil pitches about a point x_p as measured from the leading edge; all experiments here were done for $x_p = c/2$ where c is the chord length. The heaving amplitude is $h_0 = 0.5c$, the pitching amplitude is $\theta_0 = 70°$, the aspect ratio is 2, and $Re = 20,000 - 30,000$. The freestream, U_∞ is considered uniform and constant. The hinge of the flexible leading edge segment is $x_h = c/3$ from the leading edge, and a positive leading edge angle θ_{LE} is considered clockwise. Details of the leading edge motions will be presented in the Experimental Setup.

2.2 Key Parameters and Metrics

The pitch and heave provide the foil with additional motion relative to the fluid making the pitch angle θ_p insufficient for characterizing the motion. An effective angle of attack that takes into account the heave motion is given by

$$\alpha_{eff} = \theta_p - \arctan(\dot{h}/U_\infty) \tag{2.3}$$

The geometric argument for this is shown in Figure 2.1. The pitch motion is omitted from the formulation since here the foil pitches about the mid-chord and the contribution of the pitch varies along the chord length. A feathering parameter can be defined as

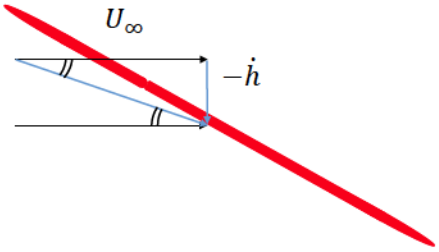

FIGURE 2.1: Geometric argument for effective angle of attack.

$$\chi = \frac{\theta_0}{\arctan\left(|\dot{h}_0|/U_\infty\right)} \tag{2.4}$$

where $|\dot{h}_0|$ is the heaving velocity amplitude. $\chi = 1$ corresponds to roughly zero net work done on the foil by the fluid. $\chi < 1$ yields thrust production in which the foil does net work on the fluid and $\chi > 1$ yields net work done by the fluid on the foil, or energy harvesting.

The ratio of the foil motion time scale to the convective time scale of the fluid is known as the reduced frequency

$$k = fc/U_\infty \tag{2.5}$$

and is a strong governing parameter for dynamic stall scenarios. As $k \to \infty$ the foil approaches flapping in quiescent air and the flow remains largely attached. As $k \to 0$ the foil motion relative to the freestream motion becomes small and the foil becomes quasi-steady; at large angles of attack flow separation will occur. When operating at large pitch amplitudes, high reduced frequencies tend to suppress stall or flow separation during the cycle [3], greatly impacting energy harvesting potential. Reduced frequency is similar to a more common parameter Strouhal number St but with a different length scale. The reduced frequencies tested in this work are $k = 0.06$, 0.08, and 0.10.

The lift force F_Y is measured in the experiments conducted here and it acts in the direction normal to the freestream, parallel to the heave motion, and is non-dimensionalized to give coefficient of lift:

$$C_Y = \frac{F_Y}{1/2\rho U_\infty^2 cb} \tag{2.6}$$

where ρ is the air density, U_∞ is the freestream velocity, c is the chord length, and b is the span. The instantaneous power harvested from the fluid is calculated from the force and moment vectors and their alignment with their analogous velocity vectors

$$P = \dot{h}F_Y + \dot{\theta}_p M \tag{2.7}$$

where M is the moment about the pivot point. At low reduced frequencies and large pitch amplitudes, the pitch contribution to power is small compared to the heave contribution [2],[4]. The reduced frequencies tested here are considered low and the contribution from the pitch is ignored.

$$P = \dot{h}F_Y \tag{2.8}$$

The cycle averaged power coefficient is given by

$$\bar{P} = \frac{1}{T}\int_0^T P dt \tag{2.9}$$

where T is the cycle period. Finally efficiency for wind energy harvesters is defined in terms of the power extracted from the flow and the theoretical energy flowing through the cross sectional area swept by the turbine

$$\eta = \frac{\bar{P}}{P_{fluid}} = \frac{\bar{P}}{\frac{1}{2}\rho U_\infty^3 bd} \tag{2.10}$$

where b is the span and d is the largest vertical distance swept by the foil.

2.3 Flapping Foil Energy Harvesters

The performance of flapping foil energy harvesters has been investigated by many authors and a synopsis of the effects of relevant parameters is presented below.

2.3.1 Reduced Frequency

As discussed above reduced frequency is a measure of how fast the foil is moving compared to the wind speed; it is one parameter that affects how much flow separation occurs and therefore influences the timing and strength of the LEV. In their parametric study Kinsey [2] reports an optimal reduced frequency range of $k = 0.12 - 0.18$ in which strong LEV shedding occurs and efficiencies comparable to rotary turbines are reached. For $k < 0.16$ power contribution due to pitch is small so as to justify neglecting the pitch component to power, an assumption that is made in this work. Zhu [4] confirmed this reduced frequency range and found an optimal reduced frequency of $k = 0.15$. Other parametric studies have identified the same optimal reduced frequency range [5], [6]. At lower reduced frequencies the LEV forms and detaches early and is unable to provide lift to the foil later in the stroke while at higher reduced frequency the growth and convection is suppressed [3],[7], [8], [9],[10].

2.3.2 Pitch Amplitude

The first flapping foil energy harvester study by McKinney and Delaurier [11] was at moderate pitching amplitudes of $\theta_0 = 25°$ and $30°$ where the highest efficiency measured was 28%. Since then it has been determined that larger pitching amplitudes are optimal; Kinsey [2] tested a range of pitching amplitudes and found that the optimal range was between $70 - 80°$; Zhu [4] confirmed this finding. High pitching amplitudes are necessary to cause LEV formation; if the pitching amplitude is low enough dynamic stall will not occur regardless of what the reduced frequency is. Varying pitch amplitude has a strong effect on the effective angle of attack whose influence on energy harvesting performance will be discussed shortly.

2.3.3 Heave Amplitude

Kinsey [2] tested only two heaving amplitudes $h_0 = 1$ and 1.5. The lower amplitude was more efficient but the higher amplitude produced a larger average power coefficient. Larger heaving amplitudes have increased power but also have larger swept areas, increasing the amount of energy available to the foil. Zhu [4] tested four heaving amplitudes $h_0 = 0.25, 0.5, 1, 1.5$ and found that $h_0 = 1$ provided the highest efficiency. Kim

[9] found an optimal heaving amplitude of $h_0 = 0.8$; the heaving amplitude should be comparable to the chord length for optimal efficiency.

2.3.4 Effective Angle of Attack

Effective angle of attack can be seen as combining the pitch and heave motions into a single parameter. Kinsey [2] found that an effective angle of attack amplitude of 35° is optimal. Kim [9] found that effective angle of attack amplitude should be between $30 - 40°$ but only for the optimal reduced frequency range. In contrast, Zhu [4] reports that efficiency increases with effective angle of attack amplitude for $k = 0.12$ and that effective angle of attack amplitude should be greater then 40° for high performance. Trapezoidal pitching profiles are beneficial for low pitching amplitudes [12] but not at optimal pitching amplitudes [13]. Larger reduced frequencies have smaller effective angles of attack which generate smaller forces, but the heaving velocity increases producing larger power. Unconventional flapping motions have also been tested [14], [15].

2.3.5 Leading Edge Geometry

Kinsey [2] reported on the effect of different leading edge geometries; no significant variation in performance was seen over NACA0002, NACA0015, and NACA0020 foils. Rival [16] found that airfoils with sharp leading edges exhibited slightly earlier LEV initiation but the growth rates were the same and the effect on performance was secondary; Kim's [9] results also support this.

2.3.6 Leading Edge Motion and Camber

Several authors have applied flexible or active control mechanisms to foils so as to mimick motions found in nature. Liu [17] found that leading edge motion improved the energy harvesting efficiency for low efffective angle of attack amplitudes by shifting the force curves to better align with the heaving velocity. Tian [18] investigated flexibility at both the leading edge and over the entire foil for the optimal parameter range, and found that neither increased the efficiency compared to the rigid case. An active control at the leading edge with reduced pitch angle did increase the efficiency. Totpal [7] found that inertial based flexibility at the leading edge does not improve efficiency or average

power coefficient for $k = 0.04, 0.06, 0.08$; it is suggested that larger forces are generated by larger leading edge tip velocities. Hoke [19] found that time varying camber with constant chord length can increase the energy harvesting efficiency at optimal operating conditions.

2.3.7 Trailing Edge Augmentation

Several authors have studied how time varying motion at the trailing edge, or other enhancements, impacts energy harvesting performance. Liu [17] determined that trailing edge motion based on a hawkmoth wing increases the lift force magnitudes and the efficiency for low pitching amplitudes. Passive trailing edge flexibility improves energy harvesting performance typically by increasing the magnitude of the lift forces [20] , [21],[22]. Gurney flaps, both fixed and adaptive, are also beneficial [23].

2.3.8 Other Considerations

Some consideration has been given for high Re where turbulence is expected . Kinsey [24] conducted CFD at Re=500,000 to study how turbulence affects the energy harvesting in 2D; they found that peak performance occurs at an effective angle of attack amplitude of 30° and that unlike the laminar case peak LEV shedding does not occur for all peak efficiency cases. 3D effects have also been investigated where reduced efficiencies are seen compared to the 2D case [25], [26]. Energy harvester prototypes have been designed and their performance compares well with numerical simulations [27]. Since energy harvesting setups would likely be installed close the ground, the effect of a shear flow as opposed to a uniform flow has been investigated [28]. The effects of the inertia of the foil have also been studied [29].

2.4 Unsteady Inviscid Vortex Models

In addition to experimental results, an inviscid discrete vortex model will be applied to the energy harvesting regimes investigated. Discrete vortex models represent shed vorticity in the wake as point vortices thereby modeling the history effects on the unsteady foil. There are several ways to model the actual foil. One way is to use conformal mapping and complex potentials to map a circle to an airfoil shape such as an infinitely

thin foil or a Joukowski foil; this is well documented by Milne-Thompson [30]. Another formulation known as thin airfoil theory assumes an infinitely thin foil where the bound vorticity distribution is modeled by a Fourier series. A final way, and the formulation chosen here, is a panel method in which the geometry of interest is built out of vortices, sources, and doublets. Both thin airfoil theory and panels methods are documented extensively in Katz and Plotkin [31].

Studies using discrete vortex models are common and have been used extensively due to their low computational cost and ability to replicate many real flow physics; some of the relevant studies are listed here. Katz [32] modeled flow separation near the leading edge using empirical data to determine the separation point for an unsteady airfoil. Ansari [33] studied insect flapping motions using a discrete vortex method coupled with the blade method where kutta conditions were applied to both leading and trailing edges. Ramesh [34] applied thin airfoil theory to airfoils with large displacements. Ramesh [1] then extended the model to incorporate shedding at the leading edge with a variable kutta condition known as the leading edge suction parameter (LESP). Liu [35] applied the Leishman-Beddos model [36] for trailing edge separation to the discrete vortex method. In addition some authors have modeled each shear layer and corresponding vortex roll up with a single point vortex that has a time varying strength [37], [38], [39].

3 Model Formulation

While high fidelity simulations have become mainstream with advances in computing power, low order simulations maintain the advantages of being much faster while still capturing the generic physics of the flow as well as being able to accurately reproducing quantities such as pressure and force. The model chosen here is a point vortex panel method applied to an infinitely thin airfoil. This method was chosen due to its simplicity compared to other panel methods that model the thickness of the foil; thickness is a secondary effect and the main focus here is on modeling the unsteady flow. Choosing a panel method over a more analytical option such as thin airfoil theory gives the flexibility to better model complexities such as camber and relative motion at the leading edge.

Consider a body moving through a fluid with horizontal translation U_∞, vertical velocity $\dot{h}$, and rotational velocity $\dot{\theta}_p$ as seen in Figure 3.1. The model is inviscid and incompressible, and the continuity equation becomes the Laplacian of the potential function Φ which is called the velocity potential [31]:

$$\nabla \times \vec{q} = 0 \tag{3.1}$$

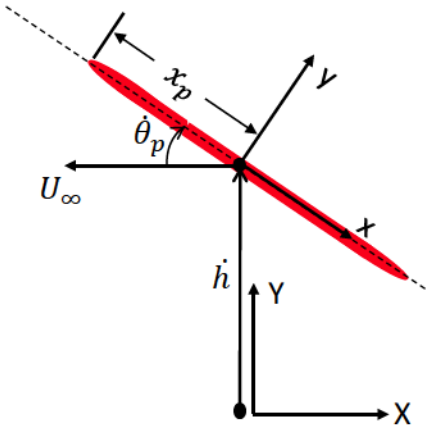

FIGURE 3.1: Airfoil motion in the inertial frame (X, Y) with the coordinate system (x, y) aligned with the foil chord.

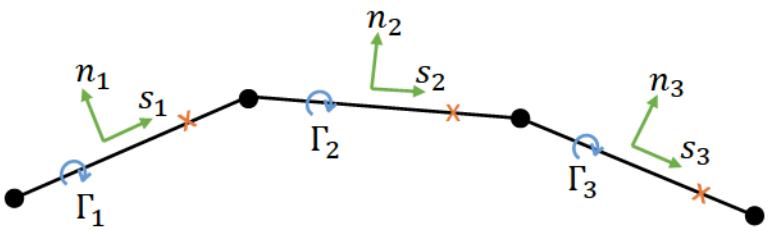

FIGURE 3.2: Airfoil discretization into panels with vortices marked at the 1/4 panel length and the collocation points at the 3/4 panel length. Also the normal-tangential coordinate system for each panel is shown.

$$\vec{q} = \nabla\Phi \tag{3.2}$$

$$\nabla \cdot \vec{q} = \nabla^2\Phi = 0 \tag{3.3}$$

The velocity vector $\vec{q}$ is induced in the otherwise quiescent fluid by the presence of the airfoil and does not include the translation or rotation of the airfoil; it is considered a perturbation potential that decays far from the airfoil [31]. Solutions to the Laplace equation can be superimposed to build other solutions and here point vortices are used to build the solutions of interest. These vortices have all their vorticity contained at the vortex center thus enabling inviscid formulations everywhere in the fluid except at the exact location of any vortex. The influence coefficients, or velocity induced by a point vortex in the x and y directions respectively, are

$$u_v = \frac{\Gamma_v}{2\pi} \frac{x - x_v}{\sqrt{(x - x_v)^2 + (y - y_v)^2}} \tag{3.4}$$

$$v_v = \frac{\Gamma_v}{2\pi} \frac{y - y_v}{\sqrt{(x - x_v)^2 + (y - y_v)^2}} \tag{3.5}$$

where Γ_v is the vortex circulation.

3.1 Steady Panel Method

Boundary element methods, or panel methods, model the inviscid flow around a body and allow for the calculation of pressures and forces acting on the body. The airfoil is discretized into n linear panels each of which contains a point vortex positioned at the 1/4 panel length and the collocation point positioned at the 3/4 panel length (see Figure 3.2). The collocation point is where impermeability is enforced; the sum of the velocity contributions normal to the surface at each collocation point is zero. This is implemented via n linear equations, one for each collocation point, where the n unknowns are the circulation of each vortex on each panel. For the steady case this yields for a collocation point i

$$\Sigma A_{ij}\Gamma_j - U_{\infty,n,i} = 0 \tag{3.6}$$

where A_{ij} is the influence coefficient of the vortex on panel j on the collocation point on panel i in panel i's normal direction and $U_{\infty,n,i}$ is the corresponding normal component of the freestream.

This system of equations implicitly encodes the Kutta condition at the trailing edge as shown in Figure 3.3. The Kutta condition states that the flow must leave the trailing edge smoothly making the pressure difference across the trailing edge zero. Here there is an implied wake panel beyond the last specified panel n with a vortex and collocation point. The pressure must be zero across this panel, and the vortex on this wake panel must have zero strength thereby making this equation trivial.

3.2 Unsteady Panel Method

In the unsteady case there are additional velocity contributions from the heaving motion, pitching motion, vortices shed from the trailing edge, and vortices shed from the leading edge. All these additional contributions are known at each time step and the equation for impermeability at a collocation point is now given by

$$\Sigma A_{ij}\Gamma_j = U_{\infty,n,i} + \dot{h}_{n,i} + (\dot{\vec{\theta}}_p \times \vec{r}_i)_{n,i} - \frac{\partial \Phi_{LEV}}{\partial n_i} - \frac{\partial \Phi_{TEV}}{\partial n_i} \tag{3.7}$$

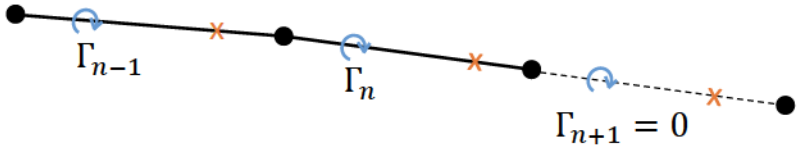

FIGURE 3.3: Illustration of implied Kutta condition and wake panel at the trailing edge.

where $\dot{h}_{n,i}$ and $(\dot{\vec{\theta}}_p \times \vec{r}_i)_{n,i}$ are the velocities induced by the foil's heave and pitch respectively; $\frac{\partial \Phi_{LEV}}{\partial n_i}$ and $\frac{\partial \Phi_{TEV}}{\partial n_i}$ are the velocity contributions from all vortices shed from the leading edge and trailing edge. The subscript n denotes the normal direction.

The coordinate systems are defined as shown in Figure 3.4 where θ_i is the panel angle relative to the chord line; for panels on the leading edge, it also encodes the instantaneous leading edge position. The rotation matrices are

$$\begin{bmatrix} u_s \\ u_n \end{bmatrix} = \begin{bmatrix} cos(\theta_p - \theta_i) & -sin(\theta_p - \theta_i) \\ sin(\theta_p - \theta_i) & cos(\theta_p - \theta_i) \end{bmatrix} \begin{bmatrix} u_X \\ u_Y \end{bmatrix} \tag{3.8}$$

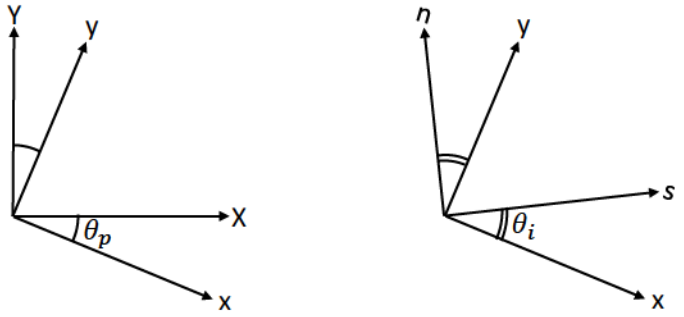

FIGURE 3.4: Inertial coordinate system (X, Y), foil coordinate system (x, y), panel coordinate system (s, n).

$$\begin{bmatrix} u_s \\ u_n \end{bmatrix} = \begin{bmatrix} cos(\theta_i) & sin(\theta_i) \\ -sin(\theta_i) & cos(\theta_i) \end{bmatrix} \begin{bmatrix} u_x \\ u_y \end{bmatrix} \tag{3.9}$$

In an unsteady flow the bound circulation changes in order to satisfy impermeability and the Kutta condition; this change in vorticity must be balanced by vorticity being shed into the fluid due to Kelvin's circulation theorem.

$$\sum \Gamma_i + \sum \Gamma_{LEV} + \sum \Gamma_{TEV} = 0 \tag{3.10}$$

At low angles of attack vorticity is only shed at the trailing edge. The shed vortex is positioned so as to approximates the shape of the shear layer; from Ansari [33] the vortex is placed at 1/3 the distance of the previously shed vortex from the trailing edge. The strength of this shed vortex is an additional unknown and its strength is solved for iteratively using a 1D newton's method as given by Katz and Plotkin [31] . The method is as follows where m is the number of vortices shed from the trailing edge and k is the newton's iteration;

1) Guess a value for the recently shed vortex Γ_m.

2) Solve Eqn 3.7 for the foil circulation Γ_i

3) Calculate the sum of all circulations $f(\Gamma)$.

$$f(\Gamma)_k = \sum \Gamma_i + \sum_{j=1}^{m-1} \Gamma_{j,TEV} + \Gamma_{m,k} \tag{3.11}$$

4) $f(\Gamma)$ must go to zero; compute an iteration of the newton's method to calculate the next guess for Γ_m.

$$\Gamma_{m,k+1} = \Gamma_{m,k} - \frac{\Gamma_{m,k} - \Gamma_{m,k-1}}{f(\Gamma)_k - f(\Gamma)_{k-1}} f(\Gamma)_k \tag{3.12}$$

5) Now the strength of the vortices on the foil must be re-calculated to enforce impermeability and the Kutta condition via Eqn (3.7). Repeat 2-5 until an appropriate residual is reached.

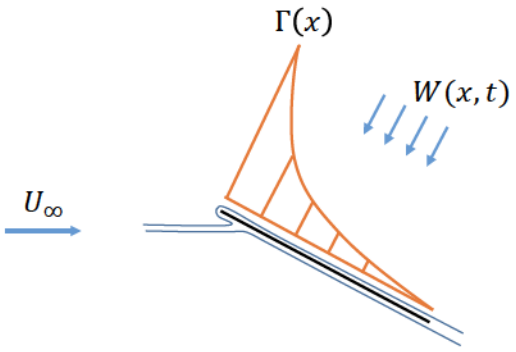

FIGURE 3.5: Depiction of a typical bound vorticity distribution due to flow perfectly navigating the leading edge, and downwash $W(x,t)$

3.3 Vortex Shedding at the Leading Edge

The parameter space studied here involves large angles of attack in which dynamic stall is encountered. Therefore it is necessary to not only shed vortices at the trailing edge but also at the leading edge to model the LEV. The problem becomes when to shed vortices and with what circulation strength. Here the model by Ramesh [1] is implemented and the Leading-Edge-Suction-Parameter (LESP) is used. This quantity comes from thin airfoil theory in which the bound vorticity is formulated in terms of a Fourier series. In order for the flow to navigate the leading edge the vorticity at the leading edge must be large as seen in Figure 3.5; therefore the first Fourier coefficient is paired with a cotangent term to provide this spike in vorticity at the leading edge.

$$\gamma(\nu,t) = 2U_\infty\left(A_0(t)\frac{1+\cos\nu}{\sin\nu} + \sum_{n=1}^{\infty} A_n(t)\sin(n\nu)\right) \tag{3.13}$$

where ν is a measure of position on the chord in a polar coordinate system with $\nu = 0$ being the leading edge and $\nu = \pi$ the trailing edge. A_0 is a measure of how large the vorticity is at the leading edge and therefore is taken to be the LESP; from Katz and Plotkin [31]

$$A_0 = -\frac{1}{\pi}\int_0^\pi \frac{W(x,t)}{U_\infty} d\nu \tag{3.14}$$

where W(x,t) is the downwash and takes into account the foil motion, freestream, and the velocity potential from the previously shed vortices:

$$W(x,t) = -(-U_{\infty,n,i} - \dot{h}_{n,i} - (\dot{\vec{\theta}}_p \times \vec{r}_i)_{n,i} + \frac{\partial \Phi_{LEV}}{\partial n_i} + \frac{\partial \Phi_{TEV}}{\partial n_i}) \tag{3.15}$$

The LESP can be thought of as a modified angle of attack that takes into account not only foil motion but also history effects from the wake. Ramesh hypothesized that an airfoil has a critical LESP value for a given Re and foil geometry; the critical value is preferably determined from CFD by looking for the first instance of separation at the leading edge. When this critical value is exceeded a vortex is shed at the leading edge so as to limit the LESP to the critical value. Physically this limits the amount of vorticity or suction that the leading edge can sustain. If a vortex was shed from the leading edge at the previous time step, the current shed vortex is positioned using the same method as vortices shed from the trailing edge where the vortex is placed so as to model the shape of the shear layer. Otherwise the vortex is placed based off of the induced velocity normal to the leading edge from the freestream, heave, and pitch. To solve for the strengths of the vortices shed at the leading edge and trailing edge a 2D Newton's method is used. Eqn 3.16 given below is the updated Kelvin's circulation theorem, and Eqn 3.17 says that the LESP cannot exceed a critical value. The roots of these equations, $\Gamma_{q,LEV}$ and $\Gamma_{m,TEV}$, are found iteratively using Eqn 3.18.

$$f(\Gamma)_k = \sum_i \Gamma_i + \sum_{j=1}^{m-1} \Gamma_{j,TEV} + \Gamma_{m,k} + \sum_{j=1}^{q-1} \Gamma_{j,LEV} + \Gamma_{q,k} \tag{3.16}$$

$$f(LESP) = \begin{cases} LESP(t) - LESP_{crit} & LESP > 0 \\ LESP(t) + LESP_{crit} & LESP < 0 \end{cases} \tag{3.17}$$

$$\left|\begin{matrix}\Gamma_q \\ \Gamma_m\end{matrix}\right|_{k+1} = \left|\begin{matrix}\Gamma_q \\ \Gamma_m\end{matrix}\right|_k - \left|\begin{matrix}\frac{\partial f(\Gamma)}{\partial \Gamma_q} & \frac{\partial f(\Gamma)}{\partial \Gamma_m} \\ \frac{\partial f(LESP)}{\partial \Gamma_q} & \frac{\partial f(LESP)}{\partial \Gamma_m}\end{matrix}\right|_k^{-1} \left|\begin{matrix} f(\Gamma) \\ f(LESP)\end{matrix}\right|_k \tag{3.18}$$

$k+1$ refers to the next iteration values, Γ_q is the vortex shed at the leading edge, and Γ_m is the vortex shed at the trailing edge.

All shed vortices are assumed to convect with the inviscid velocity so as to be force free. Therefore the induced velocity from each vortex, both shed and attached to the

foil, is calculated using influence coefficients and summed up with the addition of the freestream velocity. The inviscid velocity is multiplied by the time step to calculate the increment in position.

$$x^*_{v,t+1} = x_{v,t} + \big(- U_{\infty,x} + \frac{\partial \Phi_{foil}}{\partial x} + \frac{\partial \Phi_{LEV}}{\partial x} + \frac{\partial \Phi_{TEV}}{\partial x}\big)\Delta t \tag{3.19}$$

$$y^*_{v,t+1} = y_{v,t} + \big(- U_{\infty,y} + \frac{\partial \Phi_{foil}}{\partial y} + \frac{\partial \Phi_{LEV}}{\partial y} + \frac{\partial \Phi_{TEV}}{\partial y}\big)\Delta t \tag{3.20}$$

where the '*' denotes position in the frame of reference at the current time step. All calculations are done in the foil frame and there is the additional motion of the coordinate system relative to the vortices which includes the translation of the frame due to the heave motion and the rotation of the frame due to pitch. The transformation of the vortex positions in the previous body coordinate system to the new body coordinate system is given below.

$$\begin{vmatrix} x_{v,t+1} \\ y_{v,t+1} \end{vmatrix} = \begin{vmatrix} cos(\theta_{p,t+1} - \theta_{p,t}) & -sin(\theta_{p,t+1} - \theta_{p,t}) \\ sin(\theta_{p,t+1} - \theta_{p,t}) & cos(\theta_{p,t+1} - \theta_{p,t}) \end{vmatrix} \begin{vmatrix} x^*_{v,t+1} + (h_{t+1} - h_t)sin\theta_{p,t} \\ y^*_{v,t+1} - (h_{t+1} - h_t)cos\theta_{p,t} \end{vmatrix} \tag{3.21}$$

If the calculations were done in the inertial frame this transformation is not needed.

3.4 Vortex Blob Model

Point vortices as previously discussed have infinite velocity as the center of the vortex is approached. This poses a problem since if two vortices get very close to each other, they would fling each other unrealistically; mathematically this is a time discretization issue in which the time step would have to go to zero to provide the resolution to properly integrate the velocity. The singularity at the vortex center is diffused by implementing the vortex blob model from Vatistas [40]:

$$u_v = \frac{\Gamma_v}{2\pi} \frac{y - y_v}{\sqrt{((x - x_v)^2 + (y - y_v)^2)^2 + r^4_{core}}} \tag{3.22}$$

$$v_v = \frac{\Gamma_v}{2\pi} \frac{x - x_v}{\sqrt{((x - x_v)^2 + (y - y_v)^2) + r_{core}^4}} \tag{3.23}$$

These equations replace equations 3.4 and 3.5 in calculating influence coefficients. The blob model expands the area of rotational flow to the area within the core radius r_{core} meaning that the analysis is now restricted to the domain outside of these viscous regions. Here the core radius used is $r_{core} = 1.3U_\infty \Delta t$ proposed by Leonard [41] and used by Ramesh [1]. Vortices outside of the core radius see the same influence as that from a point vortex.

3.5 Leading Edge Motion

In this work a flexible leading edge is modeled so as to determine the effect on energy harvesting performance. The leading edge is a rigid section that is attached to the rest of the wing via a hinge and undergoes arbitrary relative motion θ_{LE}. The velocity of the leading edge in the inertial frame is

$$\vec{V}_{LE} = \begin{vmatrix} 0 \\ \dot{h}(t) \end{vmatrix} + \begin{vmatrix} cos\theta_p & sin\theta_p \\ -sin\theta_p & cos\theta_p \end{vmatrix} \begin{vmatrix} \dot{\theta}_p y_{LE} \\ -\dot{\theta}_p x_{LE} \end{vmatrix} + \begin{vmatrix} cos\theta_p & sin\theta_p \\ -sin\theta_p & cos\theta_p \end{vmatrix} \begin{vmatrix} \dot{\theta}_{LE} y_{LE} \\ -\dot{\theta}_{LE}(x_{LE} - x_{hinge}) \end{vmatrix} \tag{3.24}$$

The velocity of the fluid seen by the leading edge due to the foil motion is $-\vec{V}_{LE}$ with the rotation matrix 3.8 to transform from the inertial coordinate system to the normal tangential coordinate system of each panel on the leading edge.

3.6 Pressure, Force, and Moment Evaluations

The fluid forces acting on the foil can be evaluated using either the unsteady Bernoulli equation or the momentum impulse formulation. Both will be presented here, starting with the Bernoulli's equation in the foil frame.

3.6.1 Bernoulli's Equation

From Katz and Plotkin [31]:

$$\frac{P_\infty - P}{\rho} = \frac{1}{2}\left((\frac{\partial \Phi}{\partial x})^2 + (\frac{\partial \Phi}{\partial y})^2 + (\frac{\partial \Phi}{\partial z})^2\right) + \frac{D\Phi}{Dt} \tag{3.25}$$

$$= \frac{1}{2}\left((\frac{\partial \Phi}{\partial s})^2 + (\frac{\partial \Phi}{\partial n})^2\right) - (\vec{U}_\infty + \dot{\vec{\theta}}_p \times \vec{r}) \cdot \nabla\Phi + \frac{\partial \Phi}{\partial t} \tag{3.26}$$

where s and n denote tangential and normal direction respectively, and t denotes time. Here Φ is a perturbation potential that includes the influence of vortices on the foil as well as vortices shed; it does not include the foil motion. The spatial derivative of the velocity potential is the same regardless of what frame it is evaluated in. Since the evaluation is in the foil frame, the time derivative has a convective part that takes into account the motion of the frame

$$\frac{D\Phi}{Dt} = -(\vec{U}_\infty + \dot{\vec{\theta}}_p \times \vec{r}) \cdot \nabla\Phi + \frac{\partial \Phi}{\partial t} \tag{3.27}$$

Evaluating the top and bottom sides of the foil and subtracting to get the difference in pressure across each panel yields

$$\frac{P_l - P_u}{\rho} = \Gamma(s)\left(\frac{\partial \Phi_{LEV}}{\partial s} + \frac{\partial \Phi_{TEV}}{\partial s} - (\vec{U}_\infty + \dot{\vec{\theta}}_p \times \vec{r})_s\right) + \frac{\partial}{\partial t}\int_{LE}^{s} \Gamma(s)ds \tag{3.28}$$

where $\Gamma(s)$ is the bound circulation per unit length. For an in depth derivation of equation 3.28 see the Appendix A. When a vortex is shed at the leading edge the line of integration around the foil must go past the leading edge and around this newly formed vortex. This newly shed vortex contributes to the unsteady term in Eqn 3.28 since it's strength is changing in time for the current time step. For infinitely thin foils a leading edge suction force acts at the leading edge in the chord-wise direction contributing to the lift [31].

$$F_s = \rho\pi U_\infty^2 A_0^2 \tag{3.29}$$

The total lift is given by

$$F_Y = \int_{LE}^{TE} (P_l - P_u)\cos(\theta_p - \theta(s))ds + F_s \sin(\theta_p - \theta_{LE}) \tag{3.30}$$

Here the leading edge position is encoded in $\theta(x)$. The force contribution from the pressure can be broken up into a circulatory component F_C and non-circulatory component F_{NC}

$$F_C = \rho \int_{LE}^{TE} \Gamma(s)\left(\frac{\partial \phi_{LEV}}{\partial s} + \frac{\partial \phi_{TEV}}{\partial s} - (\vec{U}_\infty + \dot{\vec{\theta}}_p \times \vec{r})_s\right)\cos(\theta_p - \theta(s))ds \tag{3.31}$$

$$F_{NC} = \rho \int_{LE}^{TE} \left(\frac{\partial}{\partial t}\int_0^s \Gamma(s)ds\right)\cos(\theta_p - \theta(s))ds \tag{3.32}$$

3.6.2 Vortex Impulse

The lift force can also be calculated based on the impulse of every vortex. From Li [42], and Bai [43] the lift force is given by

$$F_Y = \rho\sum_i (U_\infty \Gamma_i - \frac{d(\Gamma_i x_i)}{dt}) + \rho\sum_i (\frac{d(m_i y_i)}{dt}) + L_a \tag{3.33}$$

where m_i are the strength of any source terms if present and L_a is the added mass contribution. Here U_∞ is the free stream velocity in the positive X-direction, not the velocity of the foil as previously defined. In this model there are no source terms and the added mass term is considered negligible since the fluid is air. Here a vortex with a CW rotation is considered positive. Applying the force formulation yields

$$\begin{aligned} F_Y = \rho\Gamma_b(U_\infty - \frac{dx_b}{dt}) - \rho x_b\frac{d\Gamma_b}{dt} + \\ \rho\Gamma_{LEV}(U_\infty - \frac{dx_{LEV}}{dt}) - \rho x_{LEV}\frac{d\Gamma_{LEV}}{dt} + \\ \rho\Gamma_{TEV}(U_\infty - \frac{dx_{TEV}}{dt}) - \rho x_{TEV}\frac{d\Gamma_{TEV}}{dt} \end{aligned} \tag{3.34}$$

This evaluation only holds in the inertial frame. A physical understanding of each term is necessary; the 1st, 3rd, and 5th terms are the vortex lift from the bound vorticity,

vortices shed from the leading edge, and vortices shed from the trailing edge, respectively. The 2nd, 4th, and 6th terms are unsteady lift contributions from the change in bound vorticity, time varying strength of vortices shed from the leading edge, and time varying strength of vortices shed from the trailing edge respectively. The 4th and 6th terms account for the force generated by shedding vorticity at the salient edges. x denotes a position vector measured in the inertial frame. The vortex lift terms are dependent on a velocity deficit between the freestream and the inviscid velocity; As a vortex convects away from the foil its inviscid velocity approaches the freestream and it's vortex lift goes to zero [42].

The 1st, 3rd, and 5th terms are analogous to the circulatory term in the Bernoulli evaluation with the addition of the leading edge suction force, and the 2nd, 4th, and 6th terms make up the non-circulatory force

$$F_C + F_S = \rho\Gamma_b(U_\infty - \frac{dx_b}{dt}) + \rho\Gamma_{LEV}(U_\infty - \frac{dx_{LEV}}{dt}) + \rho\Gamma_{TEV}(U_\infty - \frac{dx_{TEV}}{dt}) \quad (3.35)$$

$$F_{NC} = -\rho x_b \frac{d\Gamma_b}{dt} - \rho x_{LEV} \frac{d\Gamma_{LEV}}{dt} - \rho x_{TEV} \frac{d\Gamma_{TEV}}{dt} \quad (3.36)$$

A comparison of the the Bernoulli force evaluation and the vortex impulse evaluation is given in Appendix A. All model results shown in this work were calculated using Bernoulli's equation.

3.7 Empirical Trailing Edge Separation Model

The parameter space studied here includes the low reduced frequency range in which flow separation at the trailing edge is anticipated. It is expected that the model as is currently presented would overpredict the forces [1], [44]. Liu [20] applied the empirical flow separation correction model formulated by Beddoes and Leishman [36] with some extensions from Fan [45] to flapping foils at moderate reduced frequencies.

This model calculates a deficiency coefficient that is applied to the calculated forces rather then adjusting the computed flow. A fictitious separation point along the chord is calculated from static airfoil data. This fictitious separation point $f_{0,sep}$ is a function of angle of attack for steady flow:

$$f_{0,sep} = \begin{cases} 1 - 0.3\exp(\frac{|\alpha_{eff}| - \alpha_1}{S_1}) & |\alpha_{eff}| < \alpha_1 \\ 0.04 + 0.66\exp(\frac{\alpha_1 - |\alpha_{eff}|}{S_2}) & |\alpha_{eff}| \geq \alpha_1 \end{cases} \tag{3.37}$$

where α_1 is the break angle at which the static foil reaches its maximum lift coefficient, S_1 describes how gradually the force deviates from the small angle slope, and S_2 describes how quickly lift is lost beyond the break angle. Here the empirical values are taken from Liu [35] for a NACA0015 foil with $\alpha_1 = 15.25°$, $S_1 = 3$, and $S_2 = 2.3$. The force correction is only applied to the circulatory force and suction terms.

$$C_{N,sep} = C_{N,circ}\left(\frac{1 + f_{0,sep}^{1/2}}{2}\right)^2 \tag{3.38}$$

$$C_{s,sep} = C_s(f_{0,sep})^{1/2} \tag{3.39}$$

where $C_{N,sep}$ and C_N is the adjusted and unadjusted circulatory normal force coefficient respectively, and $C_{s,sep}$ and C_s is the adjusted and unadjusted suction force coefficient respectively. In the unsteady case a first order lag is applied to the separation point

$$\tau_1 \frac{df_{sep}}{dt} + f_{sep} = f_{0,sep}(\alpha_{eff} - \tau_2 \dot{\alpha}_{eff}) \tag{3.40}$$

where τ_1 and τ_2 are relaxation constants and the argument for $f_{0,sep}$ is effective angle of attack adjusted to account for the changing boundary layer [20]. The relaxation constants are taken from Liu [35] with $\tau_1 = 0.52c/U_\infty$ and $\tau_2 = 4.5c/U_\infty$. The total adjusted lift is calculated as

$$C_Y = (C_{N,sep} + C_{N,non})\cos\theta + C_{s,sep}\sin\theta \tag{3.41}$$

where $C_{N,non}$ is the unsteady contribution from the changing bound circulation. Note that the model only reduces the circulatory and the leading edge suction contributions, not unsteady contributions. When evaluating $C_{N,sep}$ and $C_{s,sep}$ for the unsteady case f_{sep} is used instead of $f_{0,sep}$.

4 Experimental Setup and Data Reduction

Here the facilities, equipment, experimental procedure, and data processing methods will be presented.

4.1 Experimental Setup

4.1.1 Test Facilities

All experiments were conducted at a closed loop recirculating wind tunnel at Oregon State University with a cross sectional area of 1.37m x 1.52m and turbulence intensity of less then 1%. The foil was oriented vertically between end plates so as to eliminate the influence of gravity and suppress 3D effects. The gap distance between the end plates and foil were 5mm on one side and 10mm on the other side. A FlowKinetics LLC FKT 3DP1A Manometer was used to determine the freestream velocity U_∞, and density ρ.

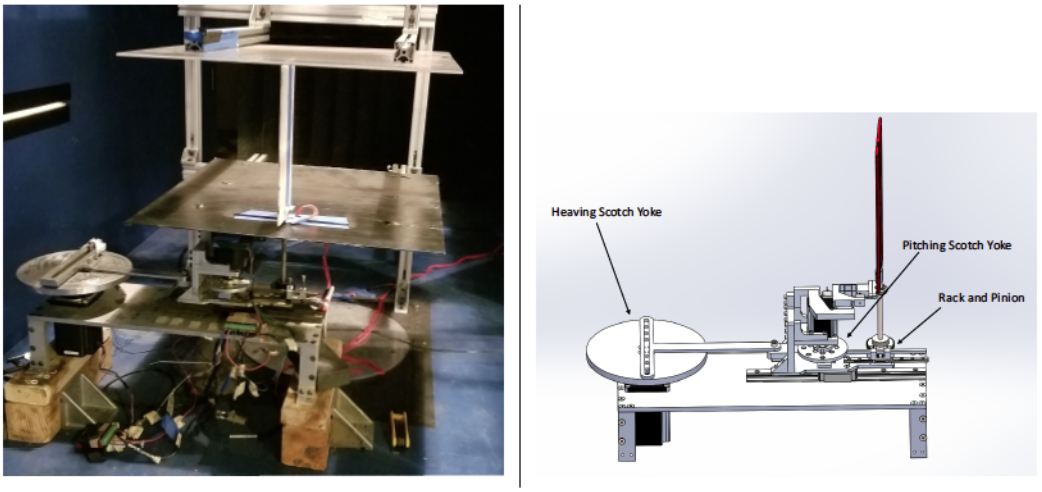

FIGURE 4.1: Device situated in the wind tunnel test section and model of device with pitching and heaving mechanisms identified.

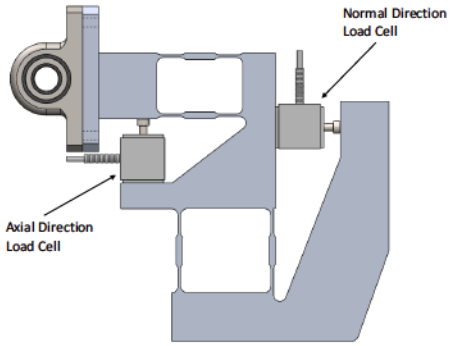

FIGURE 4.2: Custom built flexural device to minimize cross talk between load cells in axial and normal directions.

4.1.2 Flapping Foil Device

The motion device is custom built and consists of a scotch yoke mechanism to generate the heave motion, and a scotch yoke along with a rack and pinion to generate the pitch motion. The device setup in the wind tunnel and the pitching and heaving mechanisms are shown in Figure 4.1. The motors driving the heaving and pitching mechanisms are G734-1280-4 and G723-400-4 stepper motors from Gecko Drive respectively, with each controlled by a G203V motor driver. The forces during the cycle were measured using LSB200 load cells from Futek. Two load cells were used, one to measure the axial load, or drag, the other to measure the normal load, or force in the lift direction; the force in the lift direction includes both the lift and the inertial heaving forces. The load cells were installed in a custom built flexural device meant to minimize cross talk and shown in Figure 4.2.

4.1.3 Airfoil

The airfoil consists of a titanium rode and 3D printed sections as shown in Figure 4.3. The 3D printed sections were designed so as to leave the inside of the foil hollow to reduce the mass; steel stiffening rods were inserted in the chord-wise direction to make the foil stiff. the leading and trailing edges were elliptical with a major to minor axis ratio of 6:1 and the aspect ratio of the foil was 2. The chord is $c = 150mm$ and the thickness of the wing is $6.5mm$. The foil has two configurations, one being rigid, the other with a motor installed to provide active control on the leading edge. The rigid configuration has stiffening rods inserted from leading edge to trailing edge along the

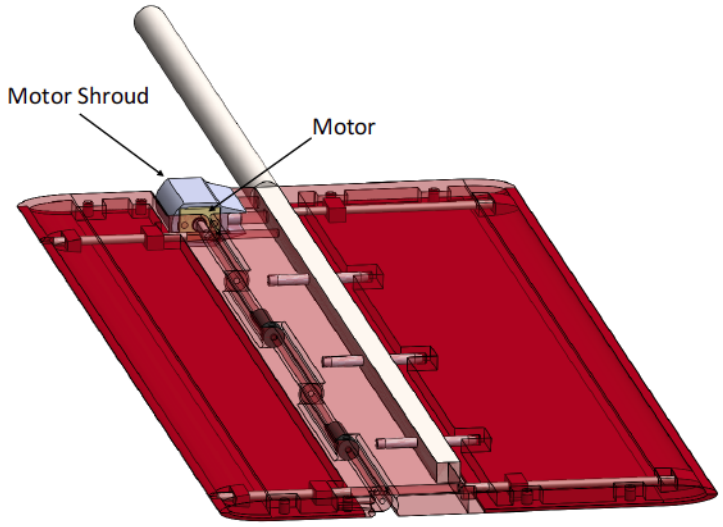

FIGURE 4.3: Wing with motor (yellow) and motor shroud (grey) identified.

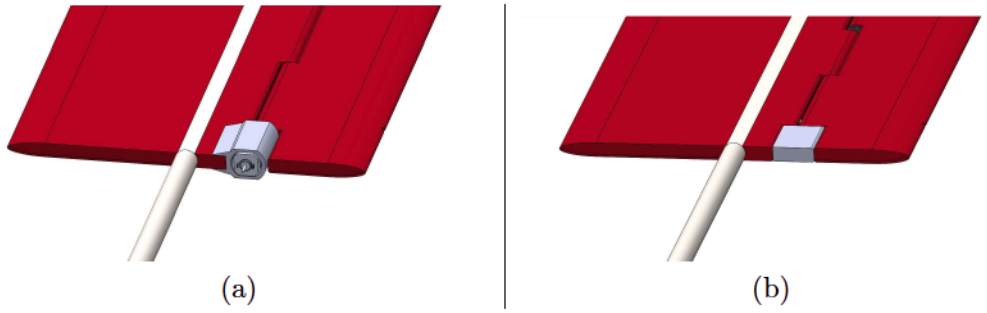

FIGURE 4.4: (a) Wing with the motor installed, (b) Wing without the motor installed.

chord and a flat segment to occupy the space where the motor would otherwise be. The motor is inserted into a 3D printed shroud that mechanically attaches to the wing and the d-shaft of the motor inserts into the leading edge segment. Models of the rigid and active control configurations are shown in Figure 4.4. The shroud provides an easy way to install the motor and also reduces the effect of the bluff geometry on the flow over the wing. The motor shroud has a thickness of $14mm$. The motor controlling the leading edge is a brushed DC Micro Metal Gearmotor HPCB 12V with a 150:1 gear box ratio from Pololu. An accompanying magnetic encoder provided position tracking with $+/-0.2°$ resolution.

4.1.4 Data Acquisition

All motion control and data collection was done using LabVIEW 2013. All data was filtered by an in house built signal processor and collected at a sampling rate of 200Hz; the position of the foil was determined by a digital signal activated mid-way through the upstroke. The leading edge motor was controlled with a digital signal due to hardware limitations; the motor was either on at the set voltage or off thus providing impulsive motion at the leading edge. The details of this motion will be discussed shortly.

As stated above the load cells were installed in a flexural device to minimize cross talk between the two force directions. From Totpal [46] the cross talk was minimized by calibrating the matrix coefficients in LabVIEW

$$\begin{vmatrix} F_N \\ F_A \end{vmatrix} = \begin{vmatrix} M_{V_N on F_N} & M_{V_A on F_N} \\ M_{V_N on F_A} & M_{V_A on F_A} \end{vmatrix} \begin{vmatrix} V_N - V_{N,0} \\ V_A - V_{A,0} \end{vmatrix} \tag{4.1}$$

where F_N is the force in the normal direction, F_A is the force in the axial direction, V_N is the normal direction voltage from a non-zero force in the normal direction, V_A is the axial direction voltage from a non-zero force in the axial direction, and $V_{N,0}$ and $V_{A,0}$ are voltages in the normal and axial direction respectively for no loading in any direction. A static tarr test was conducted for this calibration as described by Totpal [46].

4.1.5 Experimental Procedure

The wind tunnel is off. The foil is put into the mid upstroke position and if the foil is configured for leading edge actuation, the leading edge is returned to $\theta_{LE} = 0$ so that it is aligned with the rest of the foil. The physical frequency f and the phase difference between the pitch and heave are set in LabVIEW. Then the foil is set into motion. If the foil is in the actuated leading edge configuration a video of the motion is taken at $240fps$ at $720p$ resolution. The wind tunnel door is then closed; once one minute has passed since the beginning of device motion, data collection begins. This is to insure that mechanical vibrations have steady stated. Data is collected for a total of three minutes. The first minute is purely inertial forces since the wind is off; Totpal [46] showed that aerodynamic forces generated by flapping in quiescent air are negligible compared to the aerodynamic forces with the wind on for this parameter range. After the first minute, the wind tunnel is turned on. The second minute is a transient period where the freestream

is ramped up to its set value and becomes steady. Force data from the third minute is comprised of both inertial forces and the aerodynamic forces of interest. The wind is turned off and at least two minutes are allowed to pass between trials. The density is recorded to calculate lift coefficients later. $7-12$ runs are conducted for each data set. The minimum frequency used was $f = 1.25Hz$ which comes out to 75 flapping cycles per minute.

4.1.6 Data Reduction

All post processing was done in Python 3. The raw lift force data was first filtered with a 3rd order forward-backward butter filter with a cutoff frequency of $8Hz$. The data set is separated into two sub sets, one for the first minute comprising the inertial forces, and one for the third minute comprising the inertial and aerodynamic forces; the second minute is discarded. The sub set for the first minute is broken up into individual flapping cycles based on the activation of the digital signal midway through the upstroke. While the foil is going through the mid upward heave the digital signal is sent for multiple data points. The middle of this "plateau" is the true mid upward heave position and the sub data set is separated into individual flapping cycles based on this separation scheme. The physical frequency f for a particular data set is determined from this signal. The median and standard deviation are calculated across all the cycles at each time step; cycles that contain data points that fall outside of two standard deviations from the median at any time step are discarded. This is to get rid of individual cycles that deviate from the steady operation due to rare mechanical occurrences. The remaining cycles are then cycle-averaged to get a single cycle.

This process is applied to the sub data set for the third minute as well. The first minute data set is subtract from the third minute data set leaving only the aerodynamic forces; however, these aerodynamic forces are measured at the load cell and not at the mid span. In order to move the forces to the mid span the sum of moments is computed about point A in Figure 4.5.

$$F_{aero} = F_{LC}\frac{d_2 - d_1}{d_2} \tag{4.2}$$

where F_{LC} is the force measured by the load cell and F_{aero} is the aerodynamic force of interest. The lift coefficient is then calculated as given in Eqn 2.6.

4.1.7 Uncertainty Analysis

Uncertainties are calculated via the sequential perturbation method for lift coefficient, heaving power coefficient, and effective angle of attack. As stated above the forces were measured using LSB200 load cells from Futek with a rated output (RO) of $22.241N$, a non-linearity of 0.1% RO, hysteresis of 0.1% RO, and non-repeatability of 0.05% RO. From error propogation theory the total bias uncertainty is $0.033N$. The uncertainty in velocity and density from the FlowKinetics LLC FKT 3DP1A Manometer was 0.24% RO and 0.5% of the reading respectively. The span and chord were measured and a conservative estimates of $\pm 0.5mm$ were used. 95% confidence intervals were calculated over the $7-12$ data sets for each set condition; the experimental error was combined with the bias

$$x_{unc} = \sqrt{x_{bias}^2 + x_{t,95}^2} \tag{4.3}$$

where x_{unc} is the total uncertainty in x, x_{bias} is the bias uncertainty in x, and $x_{t,95}$ is the experimental uncertainty with a 95% confidence interval. Experimental uncertainty

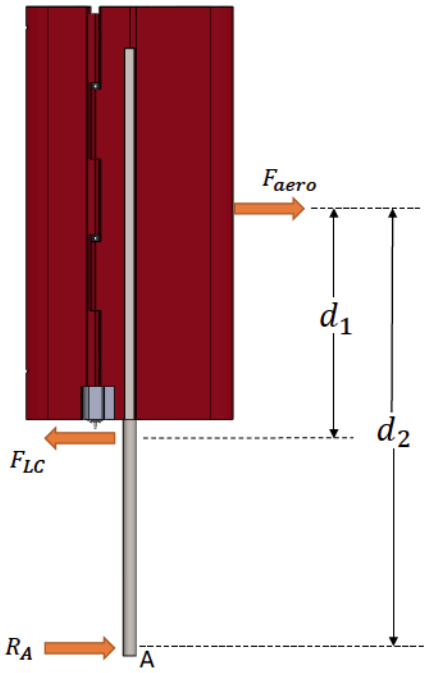

FIGURE 4.5: Force diagram to move the measured force from the load cell to the mid-span of the foil.

for force varies during the cycle due to vibration and imperfections in the mechanical mechanisms. Uncertainty values for each data point were calculated instead of an average uncertainty for the entire cycle.

To calculate the uncertainty in the power coefficient the error in heave velocity is needed. The heaving amplitude h_0 was measured by hand and a conservative uncertainty of $\pm 1mm$ was used. The error in frequency is the standard deviation of the measured frequency over all the data sets for a set condition.

To calculate the uncertainty in α_{eff} uncertainties in θ_p, θ_{LE}, the distance from the pivot point to the hinge, and the length of the leading edge segment are needed. Uncertainties for θ_p and θ_{LE} were determined by taking videos of the foil motion and tracking fudicial marks; conservative uncertainty values were $\pm 2°$. Human error in resetting the device before a data set contribute to both these errors; slop between the leading edge motor D-shaft and the leading edge segment also contributes to uncertainty in θ_{LE}. The distance from the main foil pivot to the hinge and the leading edge segment length were measured by hand and conservative values for uncertainty were $\pm 0.5mm$.

4.1.8 Leading Edge Motion Profiles

The leading edge is impulsively controlled in this setup and its length is 1/3 of the chord length. The power supply for the leading edge motor was set to 6V and 400mA current limit. The motor is controlled in LabVIEW where the inputs are the amplitude, the timing of actuation during each stroke, and the direction of the leading edge motion relative to main foil pitch. The leading edge motion is impulsive; the leading edge motor is turned on via a digital signal at the appropriate time and therefore completely off or completely on with the full voltage applied by the power supply. The LabVIEW program records the angular position of the leading edge via an encoder and when the set amplitude has been exceeded by the motion the motor is turned off. The motor and leading edge section will continue to rotate under their own inertia until friction in the hinge, motor, and gear box bring them to a halt. There is some deviation between when the motor is turned off and when the leading edge actually stops moving. The set amplitude in LabVIEW that produces the desired amplitude was determined through trial and error.

The leading edge impulsively moves from one set position to another and the timing of the motion, amplitude, and direction can be manipulated. Here the amplitude was

kept constant at 40°. There are six leading edge motions, three of which involve the leading edge rotating in the same direction as instantaneous θ_p, and three where the leading edge rotates in the opposite direction. The motions where the leading edge rotates in the same direction as the instantaneous pitch will be called positive motions. The other three motions will be called negative motions. Different positive motions have different actuation times during the stroke, and the same goes for negative motions. The visualization of these positive and negative characterization can be seen in Figure 4.6. During the downstroke when θ_p is negative,a positive motion would have the leading edge rotate counter-clock-wise ($\dot{\theta}_{LE} < 0$) at the time of actuation. Positive motions have $\dot{\theta}_{LE} < 0$ for the downstroke and negative motions have $\dot{\theta}_{LE} > 0$ for the downstroke; positive and negative motions are defined independent of the main foil pitch velocity $\dot{\theta}_p$.

The timing of the leading edge is specified in the LabVIEW program relative to the beginning of the half cycle (downstroke and upstroke). The end of the leading edge motion depends on the voltage supplied by the power supply to the motor and amplitude of the leading edge motion; the momentum of the leading edge, dynamics of the foil motion, friction in the hinge and gear box attached to the motor, and the aerodynamic force on the leading edge also impact when the leading edge comes to a halt.

In Figure 4.8 and 4.7 a schematic of the positive and negative motions are shown for the downstroke where t/T=0 is the top of the cycle and t/T=5/10 is the bottom. The

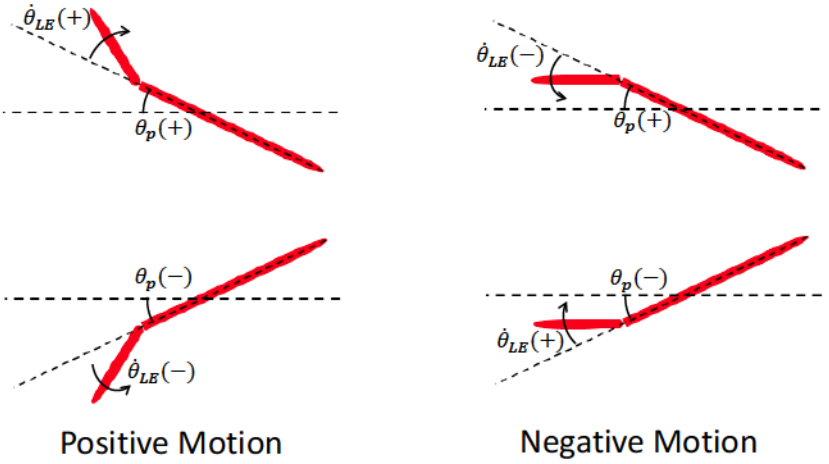

FIGURE 4.6: Positive motion in which the leading edge rotates in the same direction as the instantaneous pitch angle, and negative motion in which the leading edge rotates in the opposite direction as the instantaneous pitch angle.

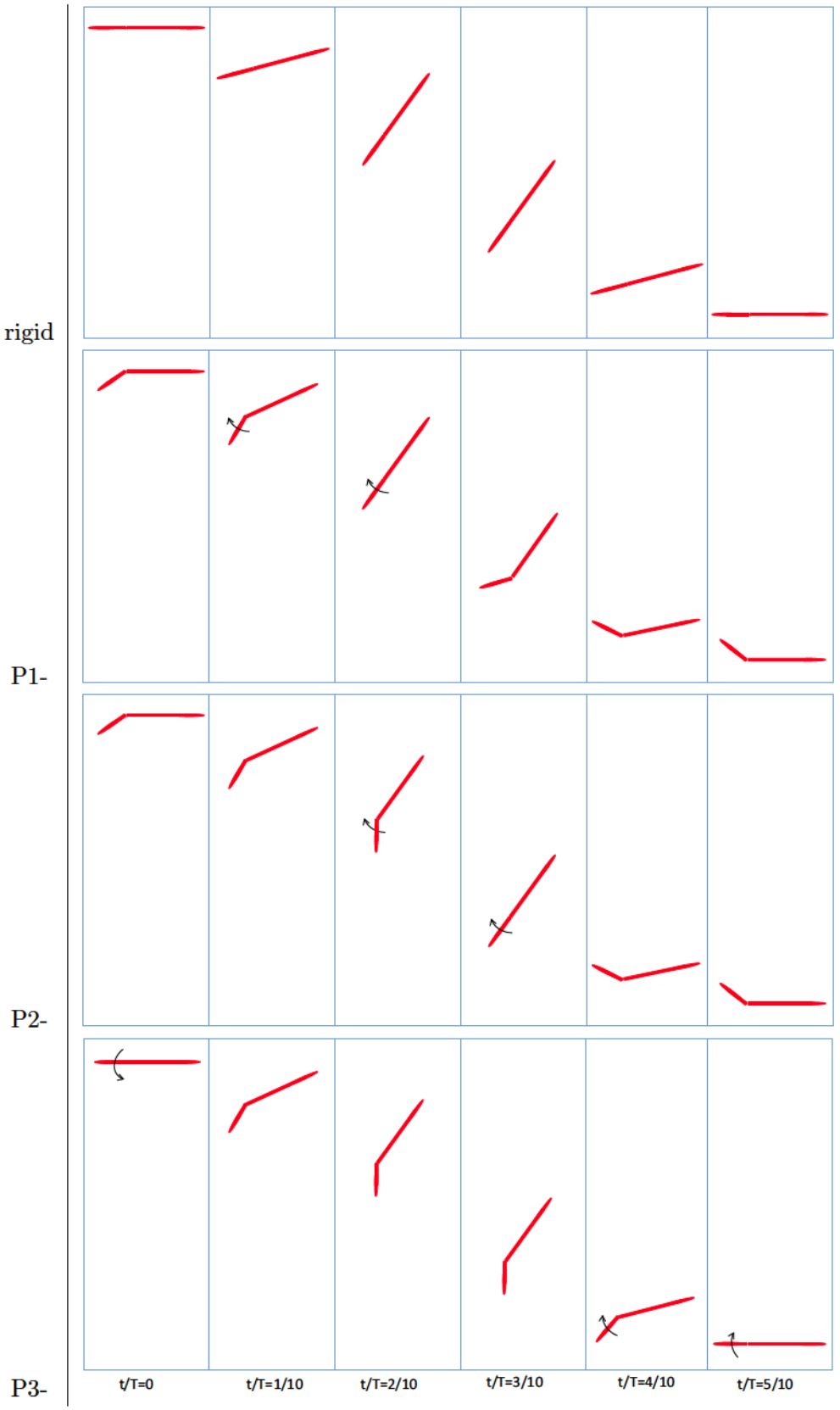

FIGURE 4.7: Leading edge during the downstroke for negative motions. The rotational arrow denotes that the LE has relative angular velocity at that instant. It should be noted that at t/T=0.1 for P3- the leading edge has just come to rest after actuating late in the upstroke.

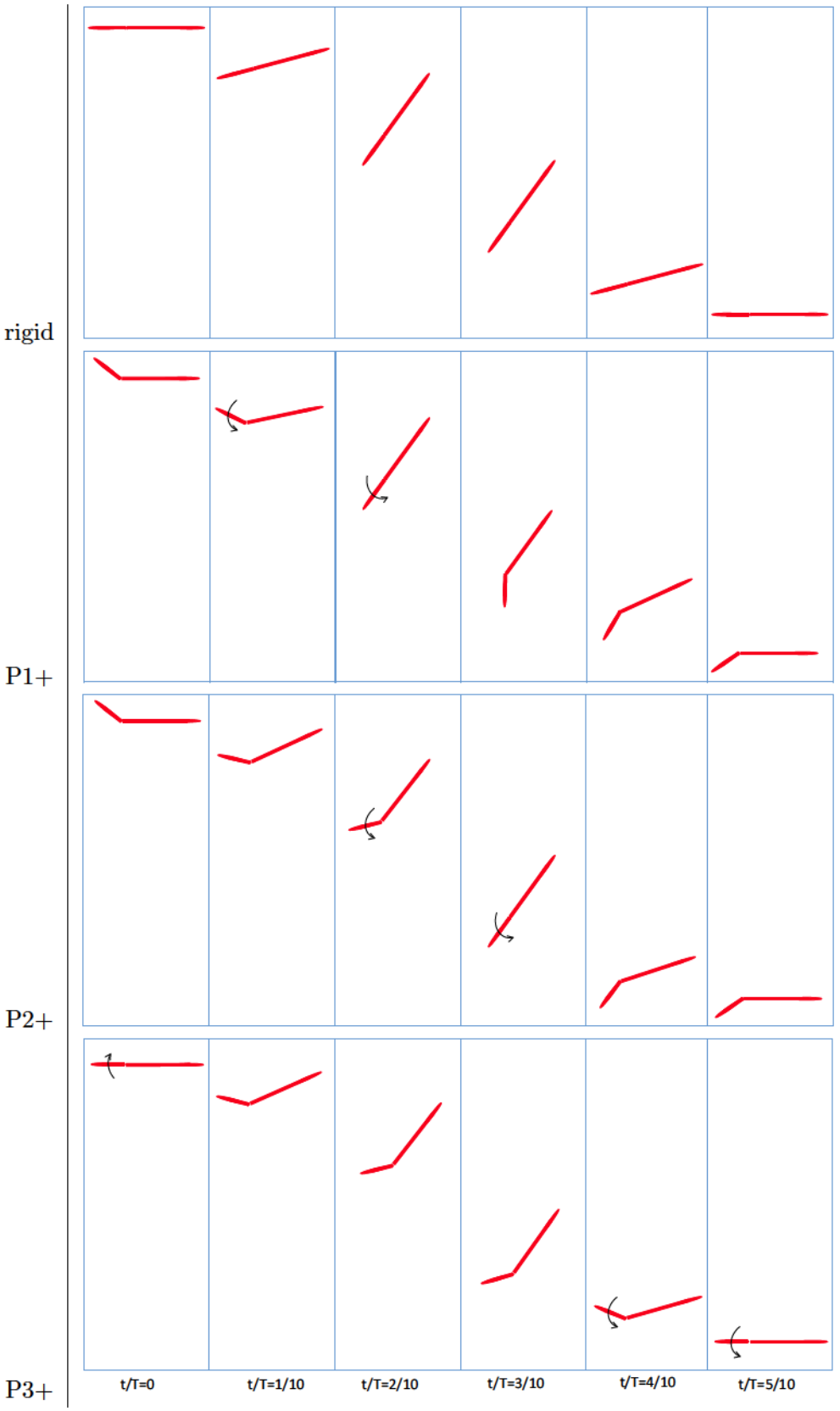

FIGURE 4.8: Leading edge during the downstroke for positive motions. The rotational arrow denotes that the LE has relative angular velocity at that instant. It should be noted that at t/T=0.1 for P3+ the leading edge has just come to rest after actuating during late in the upstroke.

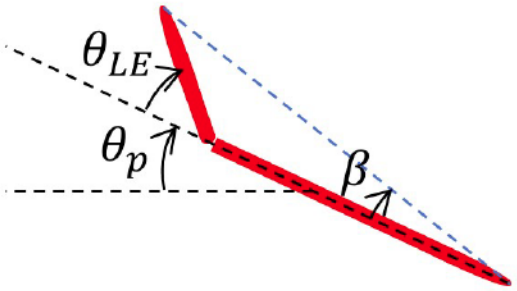

FIGURE 4.9: Camber induced by leading edge.

positive motions are P1+, P2+, and P3+; the negative motions are P1-, P2-, and P3-. The actuation time for P1+ and P1- is $t/T \approx 0.1$, for P2+ and P2- it is $t/T \approx 0.2$, and for P3+ and P3- it is $t/T \approx 0.3$. Motion times 1 and 2 are relatively early in the cycle. Motion 3 is unique in that the leading edge actuates near the end of the stroke and completes its motion early in the following stroke. Once the leading edge completes it's motion it does not return to the zero camber position and align with the rest of the foil; the leading edge maintains it's most recent position until actuated in the next upstroke or downstroke. The amplitude of the leading edge is 40° with some variation between data sets.

The trajectories of the leading edge measured by the encoder during the cycle are given in 4.10. There is no negative motion P3- data for k=0.10. Both P1+ and P1- initiate their motions at $t/T = 0.1$, P1+ with negative $\dot{\theta}_{LE}$, and P1- with positive $\dot{\theta}_{LE}$. Both P1+ and P1- finish their motions around $t/T = 0.3$. P2+ and P2- start their motions at $t/T = 0.2$ and end their motions around $t/T = 0.4$. P3+ and P3- start their motions around $t/T = 0.3$ and end their motions in the proceeding stroke at $t/T = 0.6$.

The motion of the leading edge induces instantaneous camber which is captured by a modified pitch angle

$$\theta_{eff} = \theta_p + \beta \tag{4.4}$$

where β is the interior angle formed by the camber line and the trailing edge as seen in Figure 4.9. The position of the leading edge can either add additional pitch to the foil, or decrease the pitch of the foil. A modified effective angle of attack that accounts for this camber effect is

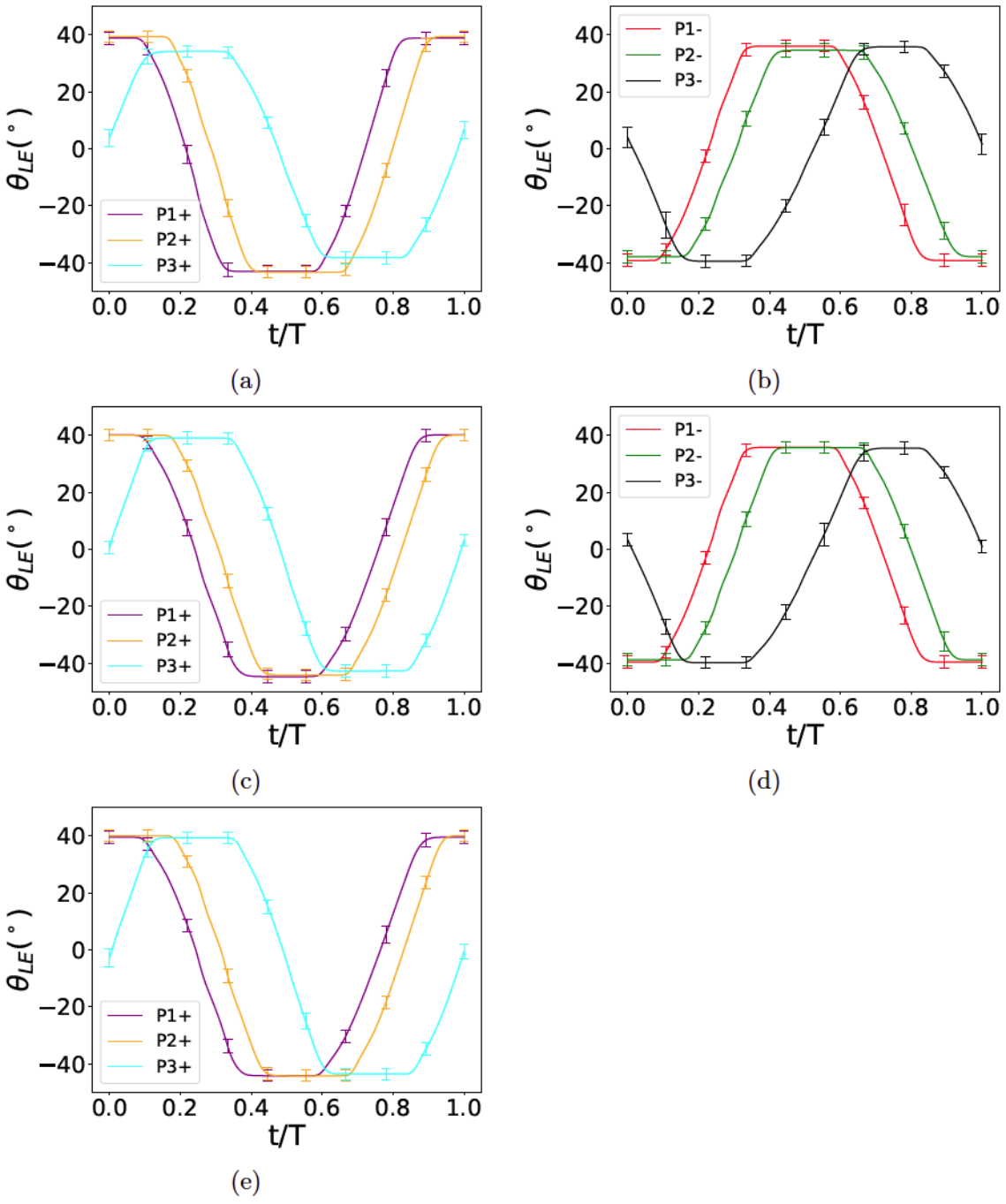

FIGURE 4.10: Deflection of leading edge during the cycle for all motions. The first, second, and third rows correspond to k=0.06, 0.08, and 0.10 respectively.

$$\alpha_{eff} = \theta_{eff} + \arctan(\frac{\dot{h}}{U_\infty}) \tag{4.5}$$

Eqn 4.5 encodes the leading edge motion and will replace Eqn 2.3 for analysis in this work.

Here additional quantities used to analyze the experimental results will be defined. It is anticipated that the performance of the flapping motion would be related to the effective angle of attack at the tip of the leading edge. The velocity of the leading edge tip in the X-direction and Y-direction in the inertial frame are respectively

$$V_{LE,X} = \dot{\theta}_p(y_{LE}cos(\theta_p) - x_{LE}sin(\theta_p)) + \dot{\theta}_{LE}(y_{LE}cos(\theta_p) - (x_{LE} - x_{hinge})sin(\theta_p)) \tag{4.6}$$

$$V_{LE,Y} = \dot{h} + \dot{\theta}_p(-y_{LE}sin(\theta_p) - x_{LE}cos(\theta_p)) + \dot{\theta}_{LE}(-y_{LE}sin(\theta_p) - (x_{LE} - x_{hinge})cos(\theta_p)) \tag{4.7}$$

The effective angle of attack at the leading edge tip is then defined as

$$\alpha_{eff,LE} = \theta_p + \theta_{LE} - arctan(\frac{V_{LE,Y}}{U_\infty - V_{LE,X}}) \tag{4.8}$$

The feathering parameter for rigid foils was given by Eqn 2.4 where the peak heaving velocity occurs during the peak pitching amplitude. For foils with time varying leading edge motion this is not the case and two new quantities are introduced.

$$\chi^* = \frac{1}{T}\int_0^T \frac{\theta_{eff}}{arctan(\dot{h}/U_\infty)}dt \tag{4.9}$$

$$\chi^*_{LE} = \frac{1}{T}\int_0^T \frac{\theta_{eff}}{arctan(\frac{V_{LE,Y}}{U_\infty - V_{LE,X}})}dt \tag{4.10}$$

where χ^* is a cycle average feathering parameter that measures over the entire cycle how effective pitch and heave induced reduction in angle of attack compare. χ^*_{LE} is a cycle averaged feathering parameter at the leading edge tip.

5 Results

Here the experimental and model results for the rigid and actuated motions will be presented. The foil pivots about the mid-chord, the heaving amplitude is $h_0 = 0.5c$, the pitching amplitude is $\theta_0 = 70°$, the aspect ratio is 2, $Re = 20,000 - 30,000$, and $k = 0.06$, 0.08, and 0.10. The leading edge is 1/3 of the chord length.

5.1 Experimental Results

5.1.1 Rigid Cases

Effective angle of attack and coefficient of lift for the rigid cases are shown in Figure 5.1. Uncertainty for effective angle of attack is high, limiting the comparison to $k = 0.06$ and 0.10. Effective angle of attack is zero at the beginning of the stroke because the foil is parallel to the flow and the heaving velocity is zero. At $t/T = 0.25$ the minimum α_{eff} is reached coinciding with the highest pitch angle and highest heave velocity. Effective angle of attack decreases with increasing reduced frequency; $\alpha_{eff,min} = -60°$ and $-50°$ for $k = 0.06$ and 0.10 respectively.

The force curves have the same basic shape across all the reduced frequencies; at $t/T = 0$ the force is negative and from there the force decreases to a primary peak, or minimum at $t/T = 0.1$. The force increases until around $t/T = 0.25$ at which time the force begins to level out; for $k = 0.06$ a saddle occurs and for $k = 0.10$ a secondary peak or local minimum occurs. The magnitude of the force is greater for the higher reduced frequency between $t/T = 0$ and 0.15. Finally the data is not symmetric between the downstroke and the upstroke for $k = 0.10$ but this deviation is small.

The power coefficient for the rigid cases are shown in Figure 5.2. Higher reduced frequencies have larger power coefficients and peak instantaneous power occurs at $t/T = 0.15$ for all cases during the downstroke. All the power coefficients begin to level out around $t/T = 0.25$ and then decrease to zero at $t/T = 0.45$.

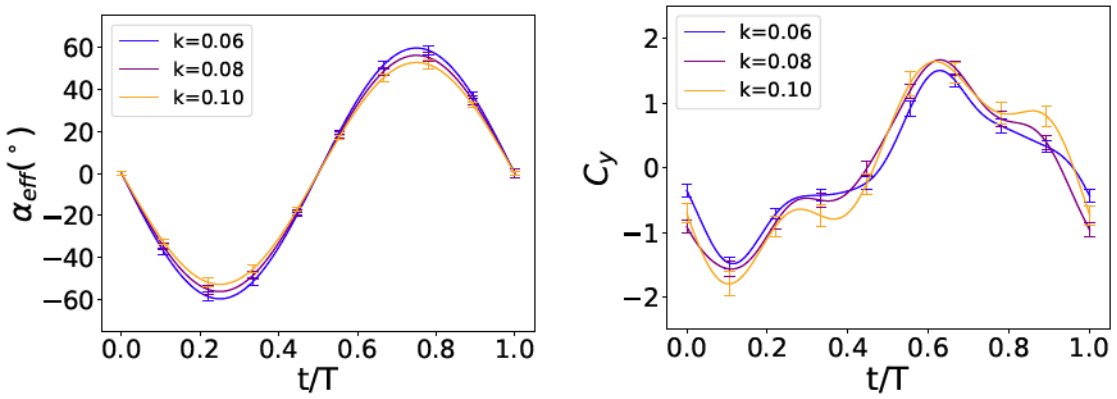

(a) (b)

FIGURE 5.1: Rigid data: a) effective angle of attack, b) lift force coefficient.

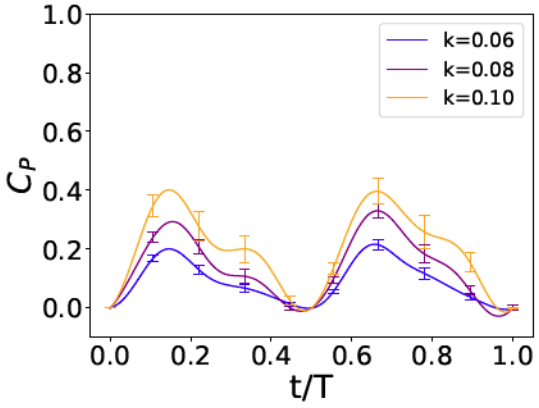

FIGURE 5.2: Rigid data power coefficient.

5.1.2 Positive Motions

Effective angle of attack and lift coefficient are shown in Figure 5.3 for the positive motions. The positive motions have reduced $|\alpha_{eff}|$ compared to the rigid case up until $t/T = 0.2$. P1+ and P2+ start at positive α_{eff} due to their camber and are decreasing at the same rate. P1+ and P2+ switch to negative effective angle of attack at around $t/T = 0.05$. They continue to decrease at the same rate until $t/T = 0.1$ when the leading edge actuates for P1+ causing $\dot{\alpha}_{eff}$ to increase (less negative) for that motion. P1+ reaches a minimum effective angle of attack at $t/T = 0.3$; for k=0.06 the value is $-68°$ and for k=0.10 it is $-56°$. P2+ reaches a minimum at $t/T = 0.32$; for $k = 0.06$ the value is $-58°$ and for $k = 0.10$ the value is $-50°$.

Both P3+ and the rigid case start at $\alpha_{eff} = 0$. P3+ exhibits a slower rate of change of effective angle of attack compared to any other motion until $t/T = 0.1$. It has the

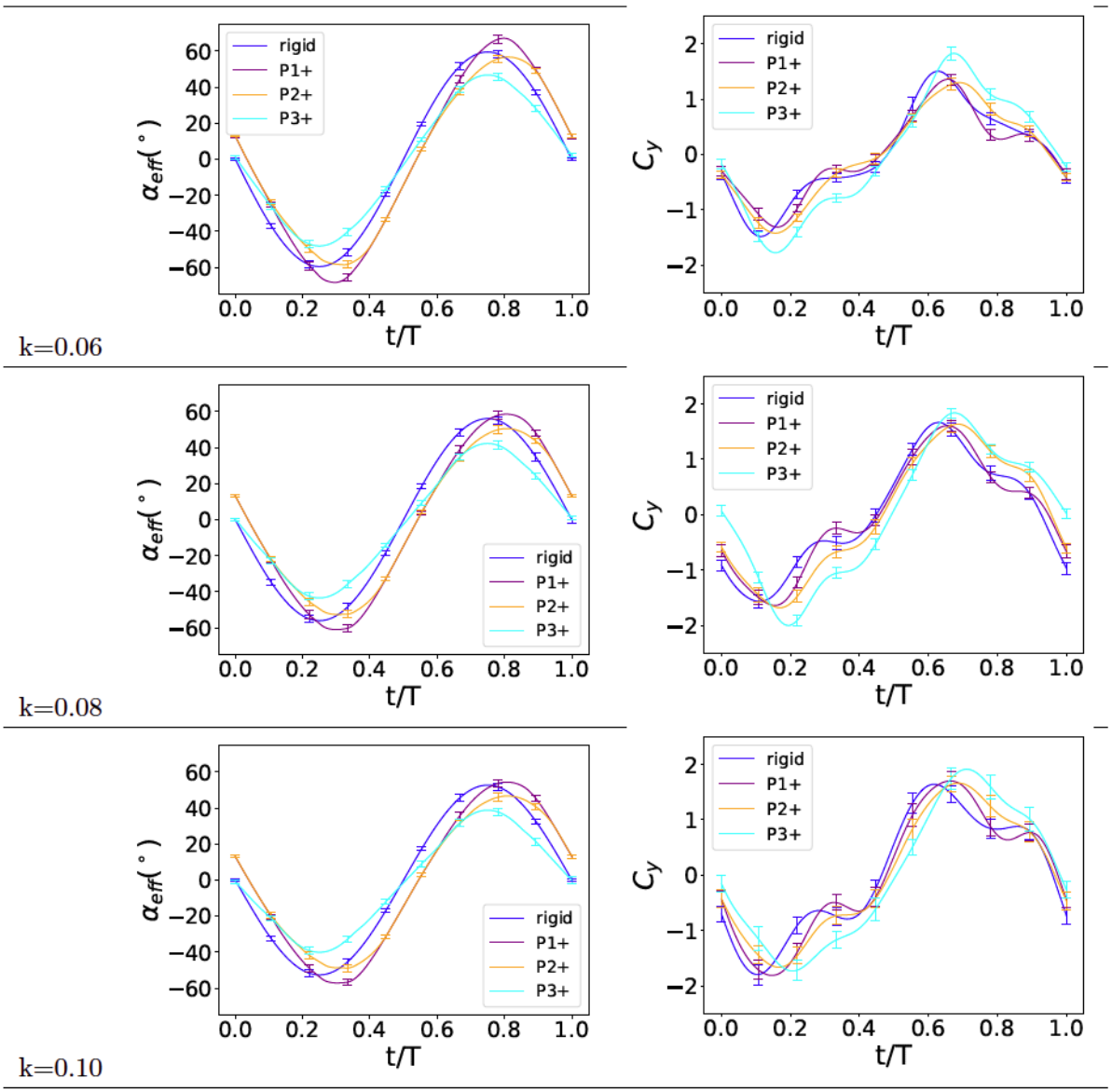

FIGURE 5.3: Effective angle of attack and lift force coefficient for positive motions. First column is effective angle of attack, second column is lift force coefficient. The first, second, and third rows correspond to k=0.06, 0.08, and 0.10 respectively.

smallest amplitude with $\alpha_{eff,min} = -50°$ for $k = 0.06$ and $\alpha_{eff,min} = -40°$ for $k = 0.10$. Additionally, the effective angle of attack amplitude occurs at the mid heave position which is the same as the rigid case.

Lift coefficients are also shown. For all motions the lift decreases to a primary peak and then increases back up to a saddle or secondary peak depending on the particular motion. For $k = 0.06$ the positive motions have primary peaks shifted later to $t/T = 0.15$ compared to the rigid case whose primary peak occurs at $t/T = 0.1$. P1+ and P2+ have

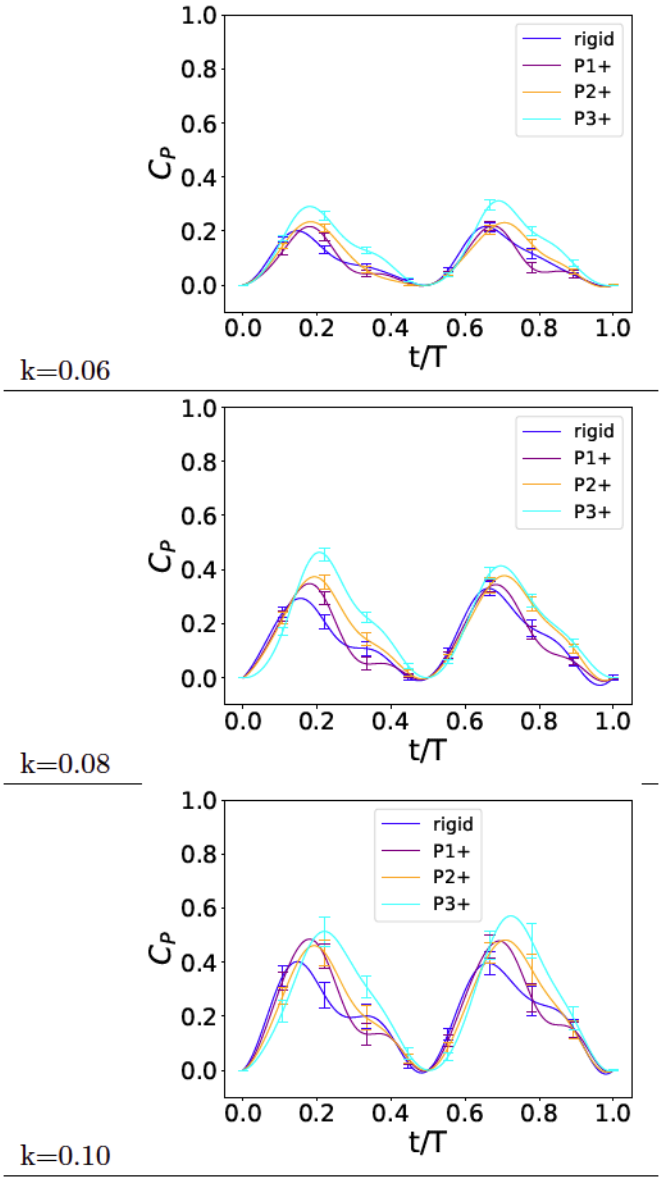

FIGURE 5.4: Heaving power coefficients for positive motions. The first, second, and third rows correspond to $k = 0.06$, $k = 0.08$, and $k = 0.10$ respectively.

primary peak values of -1.25 which are comparable to the rigid case. P3+ has a larger magnitude primary peak of -1.75 compared to all other motions. At $t/T = 0.25$ P1+, P2+ and P3+ show increasing force magnitudes of 1, 1.25, and 1.5 respectively; P3+ produces larger forces up until $t/T = 0.42$ compared to any other motion.

For $k = 0.08$, the magnitude of the force coefficients from P1+ and P2+ are smaller compared to the rigid case at the start of the downstroke; P3+ is close to zero. All actuated motions have reduced force magnitudes compared to the rigid case until $t/T = 0.1$. P1+ and P2+ have the same magnitude primary peak of 1.6 which occurs at

$t/T = 0.15$. P3+ has the largest primary peak of 2 at the latest time of $t/T = 0.2$. P1+, P2+ and P3+ show increasing force magnitudes of 1.3, 1.5, and 1.9 at $t/T = 0.22$; P3+ produces larger forces compared to any other motion up until $t/T = 0.42$

For $k = 0.10$ the primary peaks are largely comparable with values of -1.75 for the downstroke. Up until $t/T = 0.1$ the rigid case and P1+ force curves follow each other closely. At $t/T = 0.22$ the rigid case, P1+, and P3+ show increasing force values of -1, -1.5, and -1.75 respectively.

The heaving power coefficients are given in Figure 5.3. All power coefficients shown here start at zero and rise to a peak between $t/T = 0.1 - 0.3$. The power coefficients are predominantly positive. For $k = 0.06$ at time $t/T = 0.22$ the rigid case, P1+, P2+, and P3+ exhibit increasing values of $C_P = 0.12, 0.17, 0.2, 0.27$ respectively. At $t/T = 0.33$ the power coefficient for the rigid case, P1+, and P2+ are comparable with a value of 0.07.

To briefly summarize, the positive motions have their primary peaks pushed back later in the stroke compared to the rigid case. For $k = 0.06$ and 0.08, the primary peak for P3+ is larger compared to the other motions. All the positive motions have larger forces later in the cycle after the primary peak has occurred to varying degrees; P3+ has increased force magnitudes from $t/T = 0.2 - 0.45$ compared to any other motion. All the positive motions have reduced effective angle of attack magnitude up until $t/T = 0.2$ and P3+ has both the smallest rate of change of effective angle of attack early in the stroke as well as the smallest effective angle of attack amplitude.

5.1.3 Negative Motions

Effective angle of attack and lift coefficients for the negative motions are presented in Figure 5.5 for $k = 0.06$ and 0.08. For $k = 0.06$ P1- and P2-, both start at the same value of $\alpha_{eff} = -13°$ at $t/T = 0$ and share the same rate of change of effective angle of attack until $t/T = 0.1$. At this point P1- actuates, and its effective angle of attack changes more slowly. The minimum effective angle of attack for P1- occures at $t/T = 0.2$ and for $k = 0.06$ the value is $\alpha_{eff,min} = -58°$. P2- reaches a more negative value of $\alpha_{eff,min} = -66°$ and at a later time of $t/T = 0.22$.

Effective angle of attack for the rigid case and P3- both start at zero. P3- has the largest rate of change in effective angle of attack magnitude of any motion up to $t/T = 0.1$; for

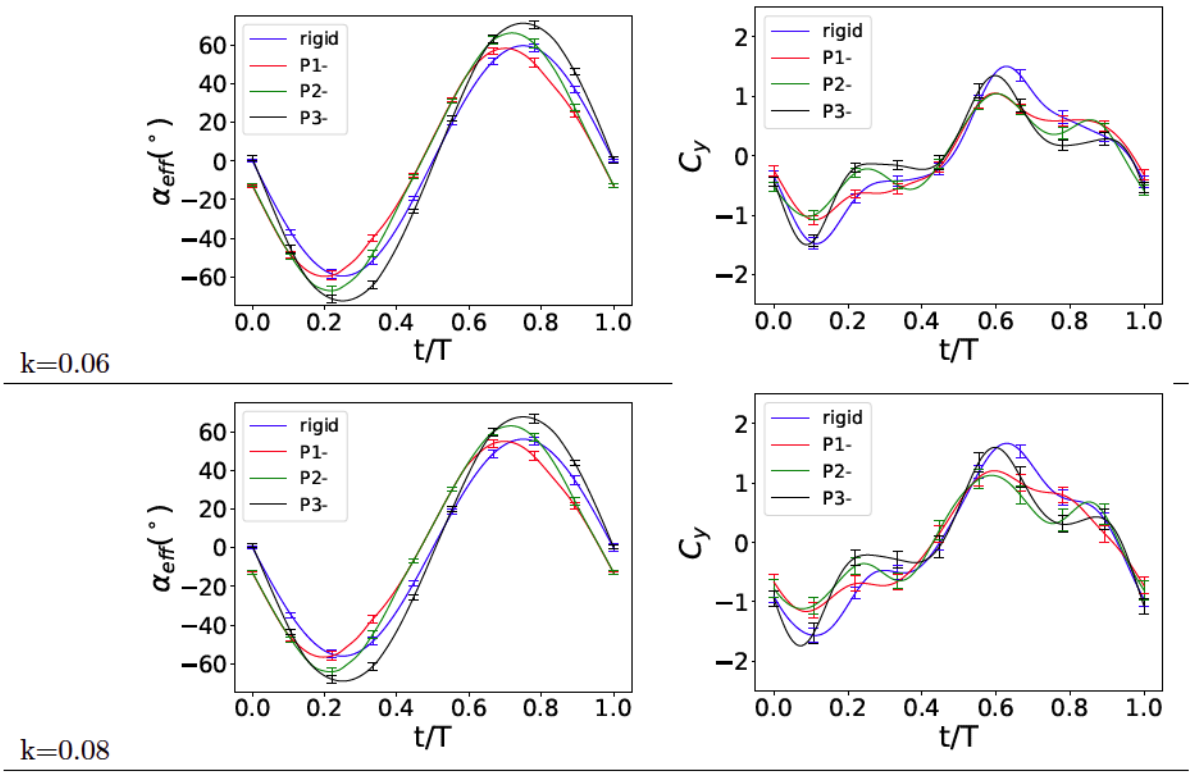

FIGURE 5.5: Force and effective angle of attack for negative motions. Effective angle of attack is given in the first column and coefficient of force is in the second column. The first and second rows correspond to k=0.06 and 0.08 respectively.

k=0.06 $\alpha_{eff,min} = -70°$, which is the largest amplitude of any motion and it occures at the same time as the rigid pitch amplitude at $t/T = 0.25$.

The force curves are also shown in Figure 5.5. P1- and P2- have smaller magnitude primary peaks compared to the rigid case while P3- and the rigid primary peak are comparable. For k=0.06, P1- increases from the minimum, or primary peak, to a saddle value of $C_Y = -0.7$ at $t/T = 0.2$ which is comparable to the rigid case. P2- increases to a local max of $C_Y = -0.3$ at $t/T = 0.25$ and then decreases to a local minimum of $C_Y = -0.6$ at $t/T = 0.37$. P3- increases up to a local max at $t/T = 0.2$ with a value of -0.2 and sees little change in lift coefficient for the rest of the stroke.

The negative motions have larger magnitudes of α_{eff} then the rigid case for $t/T = 0-0.2$ and P3- experiences larger rate of change of α_{eff} then any other motion up to $t/T = 0.1$. P2- and P3- reach larger effective angle of attack amplitudes compared to the rigid case and P3- experiences the largest $|\alpha_{eff}|$ of all motions. In the force curves P1- and P2- show smaller magnitude primary peaks compared to the rigid case while P3- has a comparable primary peak. Over the interval from $t/T = 0.25 - 0.4$, P3- has the smallest

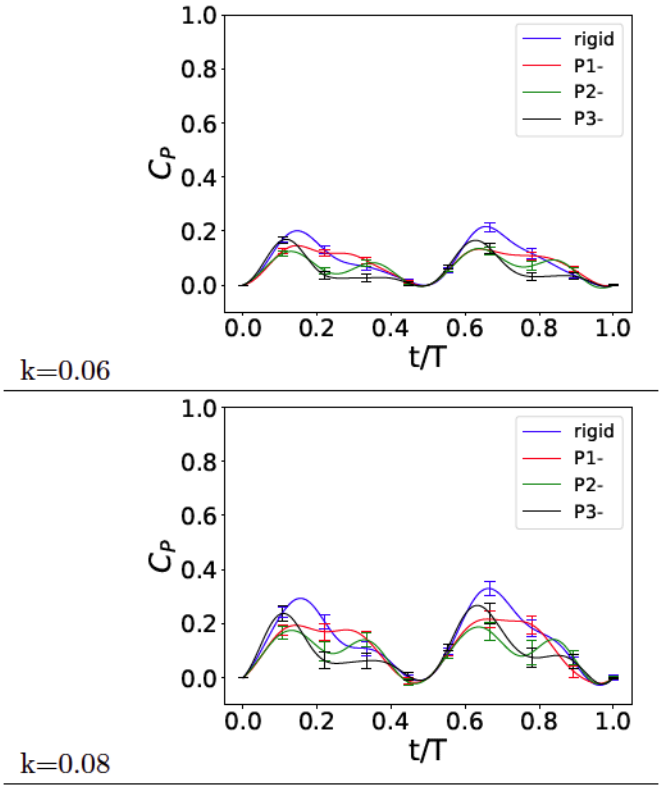

FIGURE 5.6: Heaving power coefficients for negative motions with $k = 0.06$ and 0.08 for the first and second rows respectively

force magnitudes of any motion; P1- produces forces comparable to the rigid case during this period.

The instantaneous heaving power coefficients are given for the negative motions in Figure 5.6. For $k = 0.06$, the rigid case has the largest peak power of $C_P = 0.2$ at $t/T = 0.15$. P3- follows the rigid data until $t/T = 0.1$ where the power begins to drop; by $t/T = 0.2$ the power coefficient is at a saddle of $C_P = 0.4$. P1- has reduced power compared to the rigid case up $t/T = 0.2$ at which point the power from the two motions becomes comparable. P2- shows reduced power compared to the rigid case until $t/T = 0.3$.

5.1.4 Performance Comparison Over All Data

Here the foil motions across the reduced frequencies will be analyzed using the metrics discussed in the Data Reduction section. In Figure 5.7 the heaving efficiencies for each motion and reduced frequency are shown. The rigid cases have efficiencies of 6.25%, 9.5%, and 13.75% for $k = 0.06$, 0.08, and 0.10 respectively. The negative motions show

reduced efficiencies compared to the rigid cases; P3- for $k = 0.06$ has the lowest efficiency recorded of $\eta_h = 4\%$. P2+ and P3+ produce larger efficiencies compared to the rigid cases. For the lowest reduced frequency of $k = 0.06$ P3+ shows an increase of 43% against the rigid case; for $k = 0.10$ P3+ shows an increase in efficiency of 25% compared to the rigid case.

In Figure 5.8 efficiency is plotted against effective angle of attack amplitude and effective angle of attack amplitude at the leading edge tip as defined in Eqns 4.5 and 4.8. There is a negative correlation between $\alpha_{eff,max}$ and efficiency; the largest effective angle of attack amplitude of 71° corresponds to an efficiency of 4%. The lowest effective angle of attack amplitude of 38° corresponds to an efficiency of 17.5%. The spread is wide in some areas with η_h varying from 7% to 15% at $\alpha_{eff,max} = 55°$. Efficiency is roughly correlated the same against effective angle of attack amplitude at the leading edge where now the highest efficiency of 17.5% corresponds to $\alpha_{eff,LE,max} = 42°$ and the lowest efficiency of 4% corresponds to $\alpha_{eff,LE,max} = 42°$.

In Figure 5.9 the heaving efficiencies are plotted vs the two modified feathering parameters χ^* and χ^*_{LE} as defined in Eqns 4.9 and 4.10. Heaving efficiency shows a wide spread against χ^*_{LE} with η_h ranging from 6% to 16% at $\chi^*_{LE} = 1.5$. Heaving efficiency shows a better correlation with χ^*; at $\chi^* = 2.5$ $\eta_h = 11\%$ to 15% and at $\chi^* = 4$ the efficiency ranges from 5% to 8%. Some deviation from the trend is seen at $\chi^* = 3.25$ where the efficiency ranges from 6% to 10%.

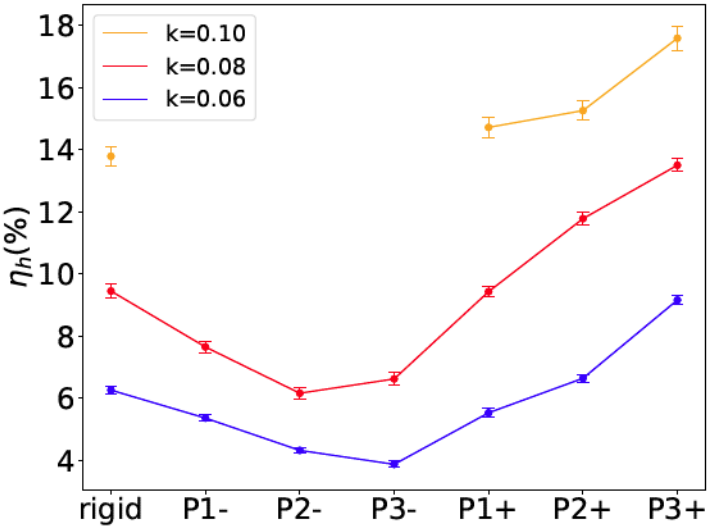

FIGURE 5.7: Efficiency based off the heaving contribution to the power coefficient.

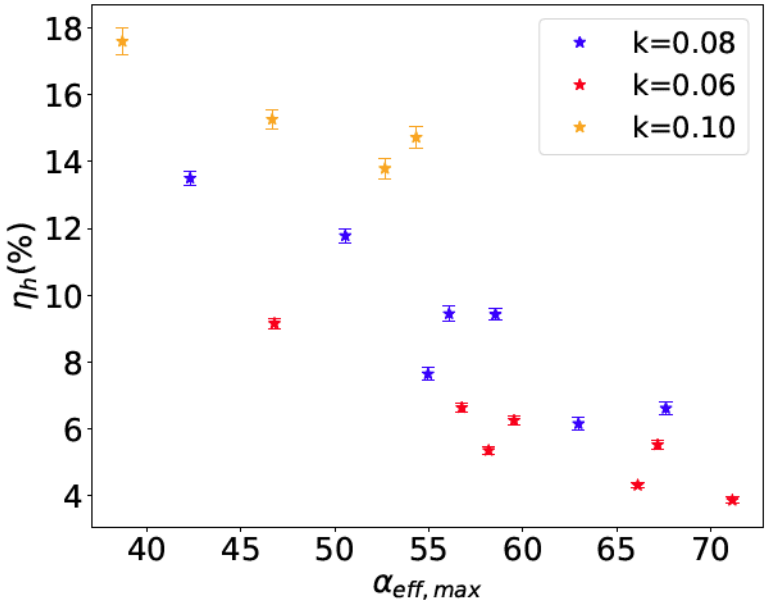

(a)

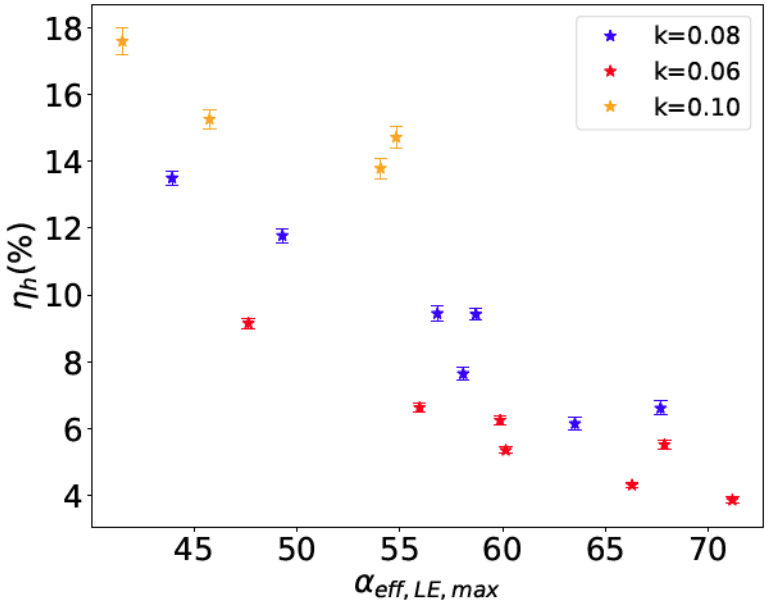

(b)

FIGURE 5.8: (a) Heaving efficiency vs. effective angle of attack amplitude. (b) Heaving efficiency vs. effective angle of attack amplitude at the leading edge tip.

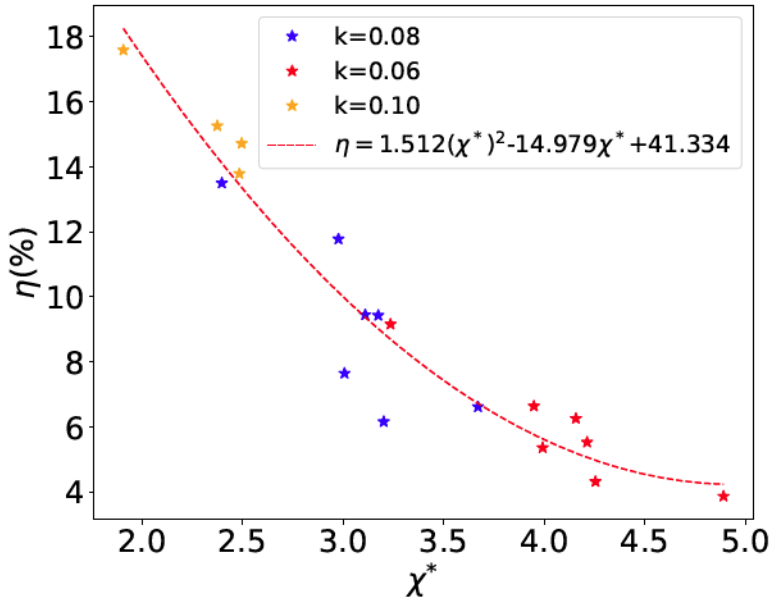

(a)

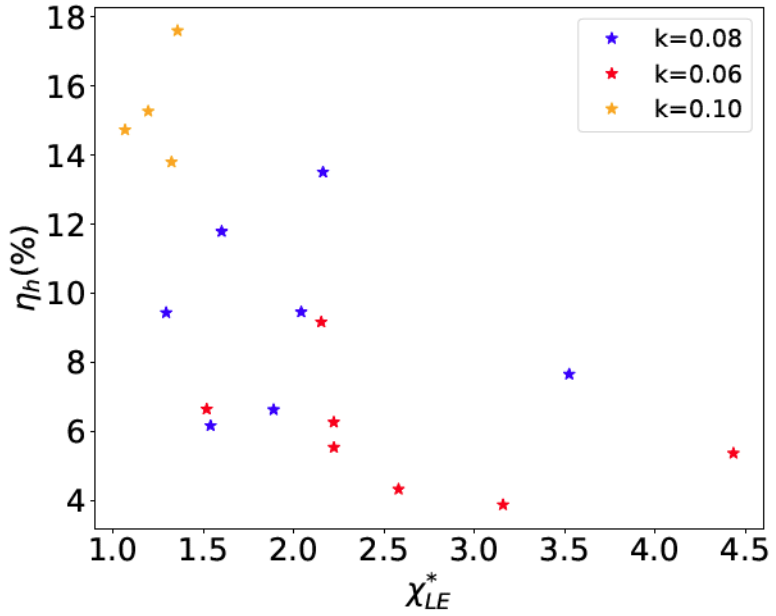

(b)

FIGURE 5.9: (a) Efficiency vs. a cycle averaged feathering parameter based on α_{eff}, (b) efficiency vs. a cycle averaged feathering parameter based on $\alpha_{eff,LE}$

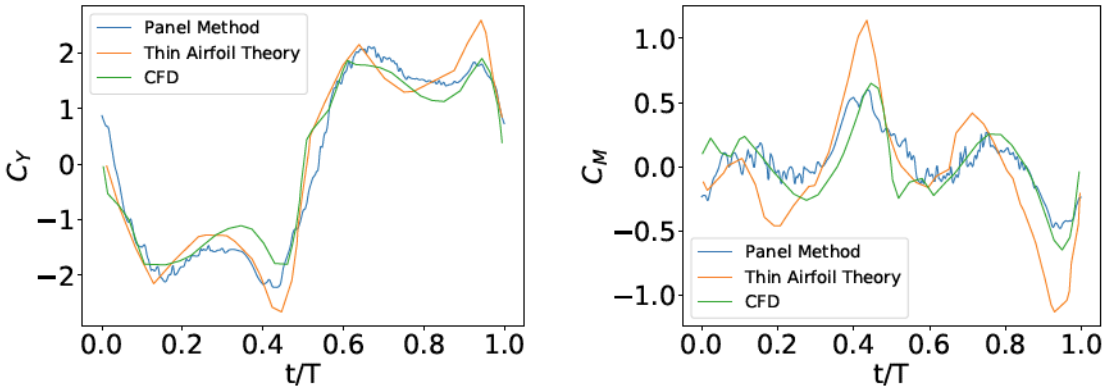

FIGURE 5.10: Comparison of panel method results to thin airfoil theory results from Ramesh [1] and CFD from Kinsey [2].

5.2 Model Results

5.2.1 Validation

The unsteady panel method with vortex shedding is compared against the thin airfoil theory from Ramesh [1] and CFD conducted by Kinsey [2] in Figure 5.10; the operating parameters are $k = 0.14$, $h_0/c = 1$, $x_p = c/3$, and $LESP_{crit} = 0.19$ corresponding to a NACA0015 foil at $Re = 1100$. At $t/T = 0$ the panel method has a force of $C_Y = 0.6$ where as both the CFD and the thin airfoil theory start at zero. The force coefficient decreases to $C_Y = -1.8$ at $t/T = 0.1$ and matches well with the CFD and thin airfoil theory. This is a minimum or primary peak and from here the magnitude of the force decreases. At $t/T = 0.3$ the panel method shows a local maximum of $C_Y = -1.5$ while the CFD has a local maximum later at $t/T = 0.375$ with a value of $C_Y - 1$; the thin airfoil theory has a local maximum slightly before the panel method with a value of $C_Y = -1.25$. All simulations then decrease down to a primary peak at $t/T = 0.45$; the thin airfoil theory shows a lift coefficient of $C_Y = -2.75$ while the panel method shows a lift coefficient of $C_Y = -2.1$ and the CFD shows a lift coefficient of $C_Y = -1.9$. Overall the panel method captures the generic trends and magnitudes. At $t/T = 0$ the panel method has a moment coefficient of $C_M = -0.25$ and for CFD $C_M = 0.2$. At $t/T = 0.1$ a peak in moment coefficient occurs with both CFD and the panel method predicting $C_M = 0.2$. The moment decreases down to $C_M = -0.25$ at $t/T = 0.25$ for both the panel method and CFD and then increases up to $C_M = 0.5$ at $t/T = 0.45$. the moment from CFD decreases more quickly from here reaching a value of $C_M = -0.25$

by $t/T = 0.5$ where as the panel method is around $C_M = 0.3$. The thin airfoil theory follows the generic trends of the CFD but underpredicts the moment at $t/T = 0.2$ and overpredicts the moment at $t/T = 0.4$.

5.2.2 LESP Analysis

Here the results from the discrete vortex model using the LESP criterion will be compared to the experimental force data. As described in the Model Formulation section, the critical LESP value is usually determined by looking at flow visualization from CFD or PIV for the first instance of shear layer rollup at the leading edge; here neither data is available and instead critical values for each case are determined by running the model for a wide range of critical LESP values and calculating the normalized root mean square (NRMS) error between the lift force predicted by the model and that from experiments. NRMS is calculated as

$$NRMS = \frac{\sqrt{\overline{(C_{l,model} - C_{l,exp})^2}}}{C_{l,exp,max}} \tag{5.1}$$

where $C_{l,model}$ is the lift coefficient calculated from the model, $C_{l,exp}$ is the measured lift coefficient, and $C_{l,exp,max}$ is the measured lift coefficient amplitude. The range of $LESP_{crit}$ is $0 - 0.4$ and 16 evenly spaced values are tested. This range was selected based on critical LESP values that Ramesh reports [1],[44]. The trailing edge separation correction is not applied to the forces produced by the model for this error minimization process; applying the trailing edge separation correction decreases the error but does not change the shape of the curves or the critical LESP at which the minimum error occurs. The NRMS errors for the positive motions and negative motions are shown in Figures 5.11 and 5.12 respectively. Only two cycles were computed where the second cycle is used in the NRMS calculation. This saves computation time while still capturing the trends and magnitudes of the force curves.

For the positive motions in Figure 5.11 the error minimization is concave up and in some cases oscillates. Most of the error curves see some degree of oscillation and this could be because the simulation has not steady stated; The rigid case at $k = 0.06$ has large oscillations for half of the critical LESP range suggesting that there is no single critical value for this motion. A Moving average with a 3 value long window was applied

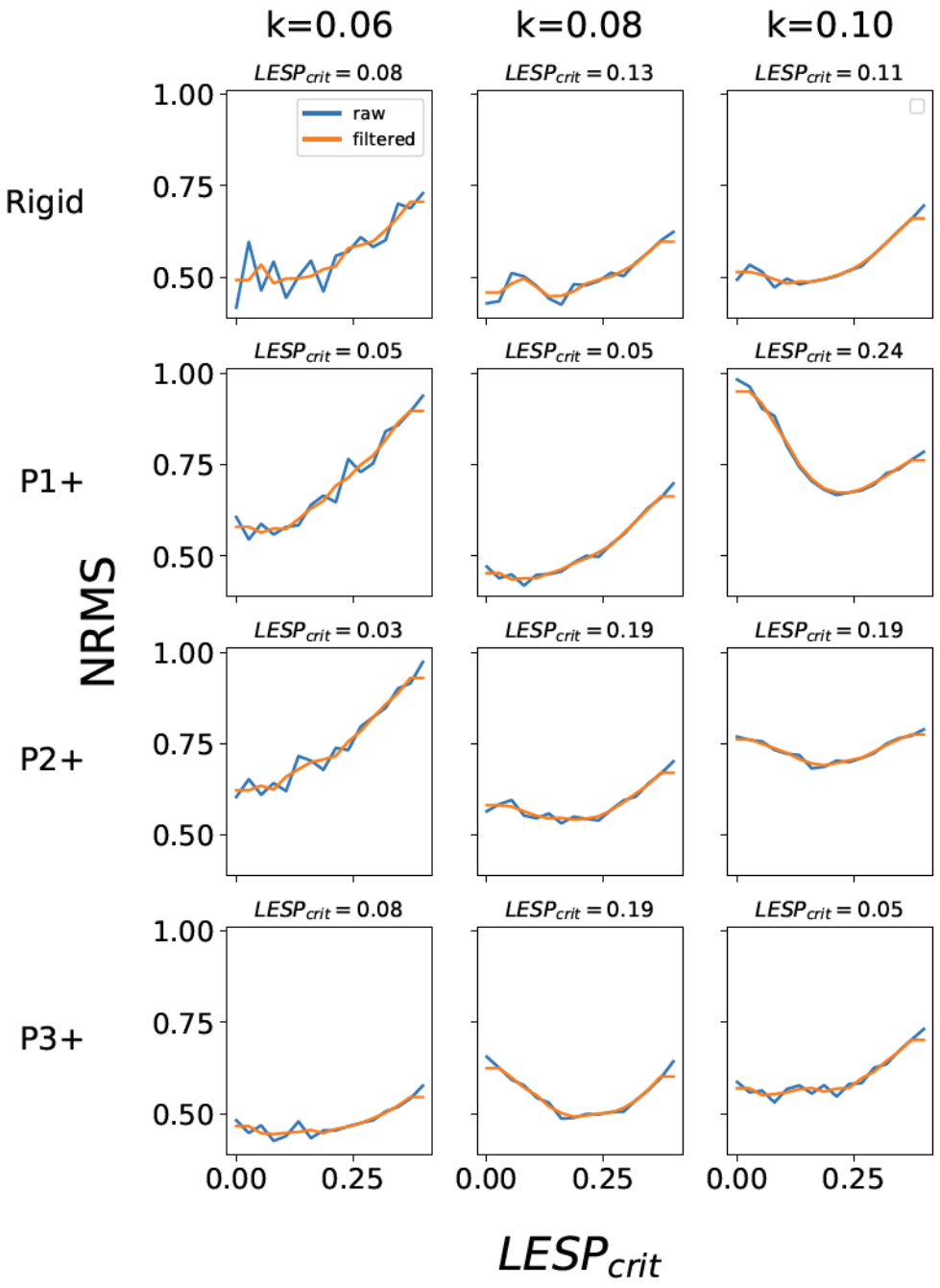

FIGURE 5.11: Error minimization to determine the critical LESP for the positive motions. The $LESP_{crit}$ value given above each plot is the value which produces the minimum error based on the filtered curve. The left, middle, and right columns correspond to k=0.06, 0.08, and 0.10 respectively. The first, second, third, and fourth rows correspond to rigid, P1+, P2+, and P3+ respectively.

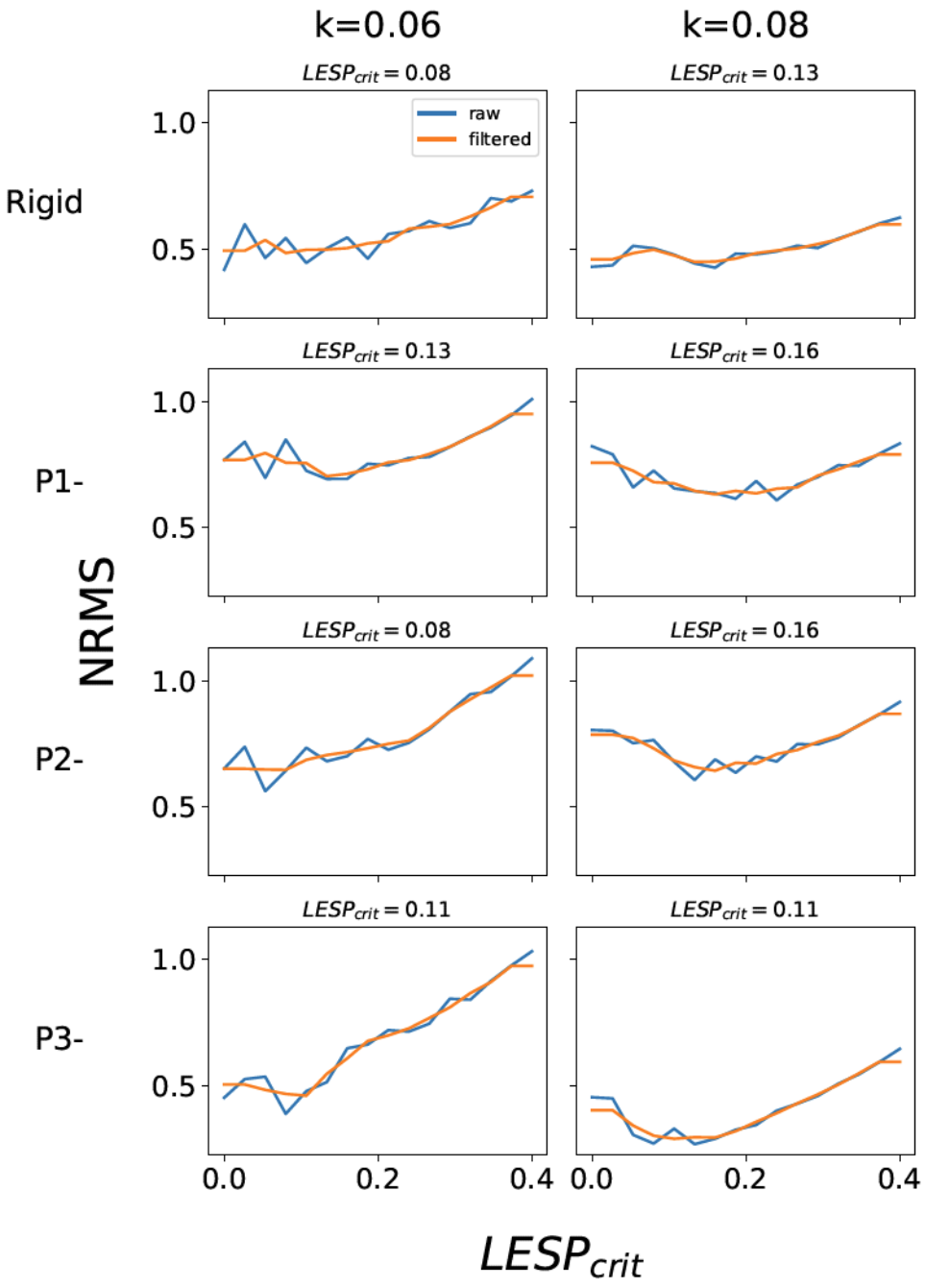

FIGURE 5.12: Error minimization to determine the critical LESP for the negative motions. The $LESP_{crit}$ value given above each plot is the value which produces the minimum error based off the filtered curve. The left and right columns correspond to k=0.06 and 0.08 respectively. The first, second, third, and fourth rows correspond to rigid, P1-, P2-, and P3- respectively.

to the error minimization and the appropriate critical LESP value for each motion was identified from this curve.

All the $k = 0.06$ motions have oscillating errors in the range $LESP_{crit} = 0 - 0.2$. P1+ and P2+ show large increases in NRMS error as $LESP_{crit}$ becomes greater then 0.1. For P3+, $LESP_{crit} = 0.08$ for the minimum NRMS and the rate of change of NRMS near this critical value is small suggesting that the coefficient of force predictions have reduced sensitivity to how much vorticity is shed at the leading edge.

P1+ for $k = 0.10$ and P3+ for $k = 0.08$ are unique in that as the critical LESP values decreases below 0.15 the NRMS error increases much more rapidly then for the other motions. The highest minimum error seen is for P2+ at $k = 0.10$ with $NRMS = 0.7$ at $LESP_{crit} = 0.24$, and the lowest minimum error seen is for P1+ at $k = 0.08$ with an error of $NRMS = 0.4$ at $LESP_{crit} = 0.05$. At $k = 0.10$, P3+ has a minimum $NRMS = 0.6$ at $LESP_{crit} = 0.05$ and the NRMS error changes very little over the critical LESP range of $0 - 0.25$. All the motions show increasing error with increasing $LESP_{crit} > 0.25$ and all but one motion has an $LESP_{crit} < 0.2$.

The LESP analysis for the negative motions is shown in Figure 5.12. The appropriate $LESP_{crit}$ are all less then 0.17 for the negative motions and NRMS increases with $LESP_{crit} > 0.17$ for all cases. P3- for both $k = 0.06$ and 0.08, have a common appropriate critical value of $LESP_{crit} = 0.11$ with $NRMS = 0.45$ and 0.3 respectively. Both P1- and P2- for $k = 0.08$ have a common appropriate critical value of $LESP_{crit} = 0.16$ and NRMS errors of 0.65. For $k = 0.06$ both the rigid case and P2- have appropriate

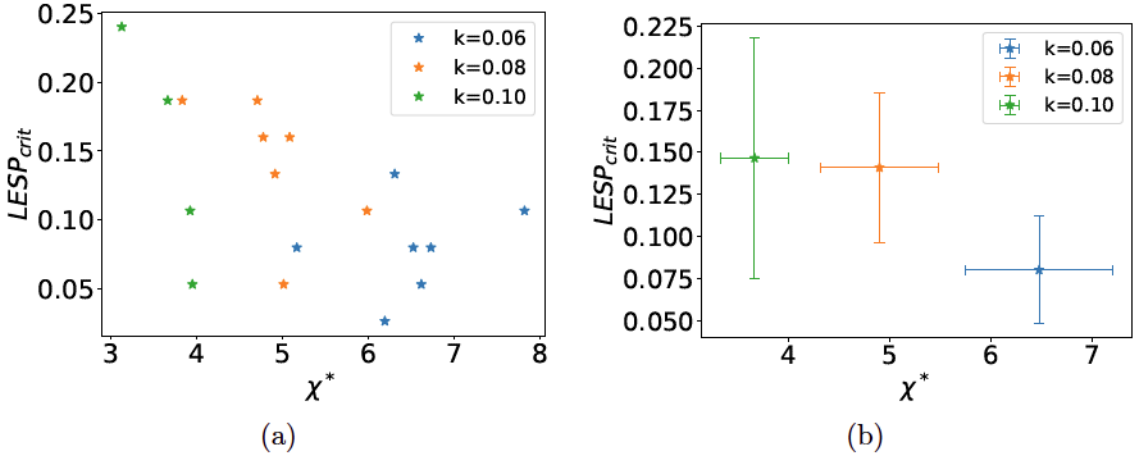

FIGURE 5.13: (a) Critical LESP that produce minimum error vs. cycle averaged feathering parameter (b) Average critical LESP for each reduced frequency where error bars denote standard deviation

critical values of $LESP_{crit} = 0.08$ with $NRMS = 0.5$ and 0.65 respectively. The lowest error observed is for P3- at $k = 0.08$ where the error is $NRMS = 0.3$ and the highest minimum error seen is $NRMS = 0.7$ for P1- at $k = 0.06$.

The appropriate critical LESP values are plotted vs cycle averaged feathering parameter in Figure 5.13; averaging for each reduced frequency across $LESP_{crit}$ and χ^* is also shown. The error bars denote standard deviation across their respective quantities. The spread is wide and there is no clear relationship between critical LESP value and χ^*. When the quantities are averaged for each reduced frequency there is a weakly correlated negative relationship between critical LESP value and χ^*. Deviation in χ^* increases with decreasing k, and deviation in $LESP_{crit}$ decreases with decreasing k. For $k = 0.10$ $LESP_{crit}$ ranges from $0.075 - 0.22$ and χ^* ranges from $3.5 - 4.2$.

5.2.3 Positive Motions, Comparison to Experimental Data

The model was run for an additional cycle at the appropriate critical LESP value for each motion and the empirical trailing edge separation correction was applied. The Force histories predicted by the model are compared against the experiments in Figure 5.14 where DVM is the force calculated from the model without the trailing edge separation correction, and DVMA is with the correction. While both DVM and DVMA are able to reproduce generic trends such as the timing of the primary peak and the secondary peak peak or saddle, both fail to predict the magnitudes of the forces. For the rigid cases there is little difference between DVM and DVMA; since the empirical force correction is only applied to the circulatory and suction contributions to the force, this suggests that these contributions are small compared to the non-circulatory contribution. For $k = 0.06$ both DVM and DVMA predict a primary peak at $t/T = 0.1$ but predict a value of $C_Y = -2.5$ while the experiment shows $C_Y = -1.5$. DVM and DVMA then increase up to a local maximum at $t/T = 0.3$ while the experiment has a saddle. The rigid case at $k = 0.08$ is similar with DVM and DVMA predicting the timing of the primary peak at $t/T = 0.1$ and the saddle at $t/T = 0.3$ but over-predicting the forces by a factor of 2.

For P1+ at $k = 0.06$, DVM follows the experiment closely between $t/T = 0.2 - 0.4$, while DVMA reproduces the primary peak better but over predicts the force later in the stroke. The same is true at $k = 0.08$. For $k = 0.10$, DVMA correctly predicts the timing of the primary peak as well as its value of $C_Y = -1.6$ but does not predict the loss of lift shown by the experiment between $t/T = 0.25 - 0.4$.

For P2+ and P3+, DVMA predicts the primary peak value better then DVM but still fails to show the decrease in lift later in the stroke; this is especially true for $k = 0.10$ where for P2+ DVM and DVMA have $C_Y = -2$ at $t/T = 0.4$ where as the experiment has $C_Y = -1$. For P3+ at $k = 0.06$ DVM follows the experiment reasonably well although it slightly over-predicts the primary peak and saddle.

Overall both DVM and DVMA overpredict the forces, and while DVMA in some instances captures the primary peak magnitude more accurately, DVM captures the shape of the force curves better. Both DVM and DVMA are unable to capture the loss of lift later in the stroke for all motions; as reduced frequency increases the model predicts larger forces later in the cycle further deviating from the experimental forces.

The circulatory and non-circulatory force contributions for the positive motions are shown in Figure 5.15. Much of the force comes from the non-circulatory part which includes the force from shedding at the leading edge. There is a peak in non-circulatory lift around $t/T = 0.1$ for all $k = 0.06$ motions and this occurs simultaneously with a minimum in circulatory force magnitude. For example the rigid case at $k = 0.06$ has a non-circulatory peak of -2.5 while at the same instant the circulatory force is close to zero. The magnitude of the non-circulatory force then decreases and the magnitude of the circulatory force increases; at $t/T = 0.3$ the circulatory force is -0.6 while the circulatory force is -0.4. Near the end of the stroke at $t/T = 0.45$ the non-circulatory force has a secondary negative peak while the circulatory force has positive peak; for the rigid case at $k = 0.06$ the circulatory force is -1 and the non-circulatory force is around 0.8.

For P1+ and P2+ at $k = 0.10$, the first peak in non-circulatory lift occurs later compared to the lower reduced frequencies; for P1+ the timing of this peak is $t/T = 0.13$, 0.15, 0.2 for $k = 0.06$, 0.08, 0.10 respectively. The same trend is seen for P2+. Many of the motions have a large secondary peak in the non-circulatory force; the rigid case for $k = 0.10$ has non-circulatory force value of -2.25 at $t/T = 0.42$. P2+ at $k = 0.08$ has a non-circulatory force of -1.75 at $t/T = 0.4$. These secondary peaks on non-circulatory force coincide with the circulatory force increasing to slightly positive values.

5.2.4 Negative Motions, Comparison to Experimental Data

The model results for the negative motions are shown in Figure 5.16 for $k = 0.06$ and 0.08. Both DVM and DVMA overpredict the forces compared to the experiments. For

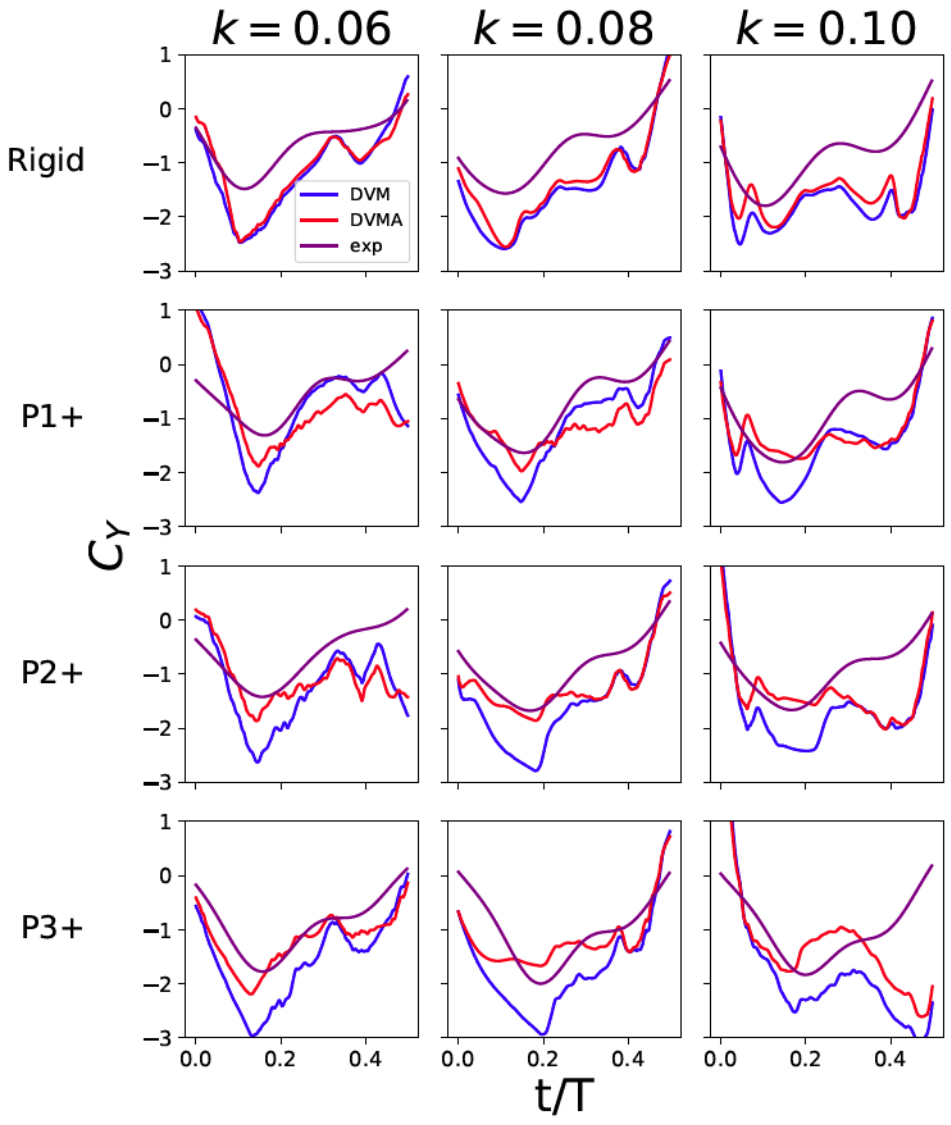

FIGURE 5.14: Comparison of lift force computed by the model, both with and without the empirical force correction, to the experimental data for the positive motions. DVM is the force predicted by the model without any empirical correction, DVMA is the force predicted by the model with the empirical force correction, and exp is the force measured from the experiment. The left, middle, and right columns are $k = 0.06$, 0.08, and 0.10 respectively. The rows correspond to the rigid case, P1+, P2+, and P3+ respectively.

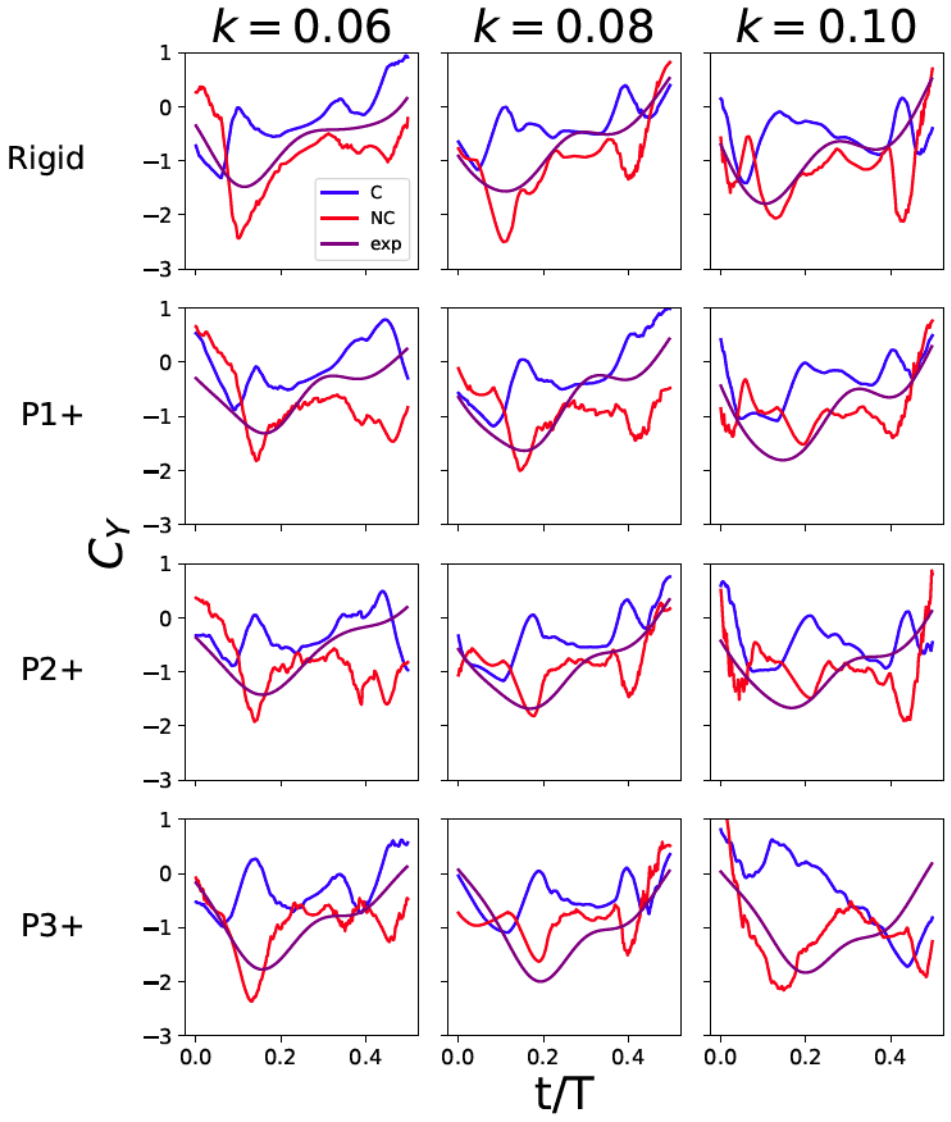

FIGURE 5.15: Comparison of the circulatory and non-circulatory forces from the model for the positive motions. C is the circulatory and NC is the non-circulatory. The total experimental lift force, exp, is also shown. The left, middle, and right columns are $k = 0.06$, 0.08, and 0.10 respectively. The rows correspond to the rigid case, P1+, P2+, and P3+ respectively.

P1- and P2- DVM and DVMA overpredict the primary peak by a factor of 2 and DVM predicts smaller force magnitudes then DVMA. DVMA compares well for P1- and P2- at $k = 0.06$ over the interval $t/T = 0.25 - 0.4$.

For P3- at $k = 0.06$ DVM follows the experimental force reasonably well between $t/T = 0.1 - 0.3$ after which it incorrectly predicts a large secondary peak while the experimental force remains small. DVM predicts smaller magnitude forces then DVMA over this range. At $k = 0.08$ DVM and DVMA reproduce the shape of the experimental forces well although both over predict the primary peak by a factory of 2. DVM better predicts the forces then DVMA.

A breakdown of the circulatory and non-circulatory force contributions for the negative motions are shown in Figure 5.17. A peak in non-circulatory force occurs early in the stroke and coincides with a minimum in circulatory force magnitude. For P2- at $k = 0.08$ the non-circulatory peak is -2.3 at $t/T = 0.3$ where as the circulatory force at this instant is close to zero. The non-circulatory force then decreases in magnitude until $t/T = 0.3$ when it either levels out to a saddle or local maximum. For most of the stroke the non-circulatory force magnitude is significantly larger then the circulatory force magnitude.

5.2.5 Modified Empirical Adjustment

It was shown in Figures 5.15 and 5.17 that the non-circulatory force contribution from the model is dominant in this parameter space. In order to better reproduce the experimental results, empirical force corrections should also apply to the non-circulatory force. Here the reduction coefficient for the circulatory force is also applied to the non-circulatory force

$$C_L = (C_{N,circ} + C_{N,non})\left(\frac{1 + f_{sep}^{1/2}}{2}\right)^2 \cos\theta + C_{s,sep}\sin\theta \tag{5.2}$$

The results from this correction are shown in Figure 5.18 for the positive motions. For the rigid cases the model predicts primary peak values of $C_Y = -1.75$, -1.6, and -1.3 for $k = 0.06$, 0.08, and 0.10 respectively which compares well with the experiments. The loss of lift later in the stroke is reproduced to varying degrees with the model showing $C_Y = -0.5$, -1.1, -1.4 at $t/T = 0.3$ for $k = 0.06$, 0.08, and 0.10. As reduced frequency increases the model deviates from the experiments later in the stroke.

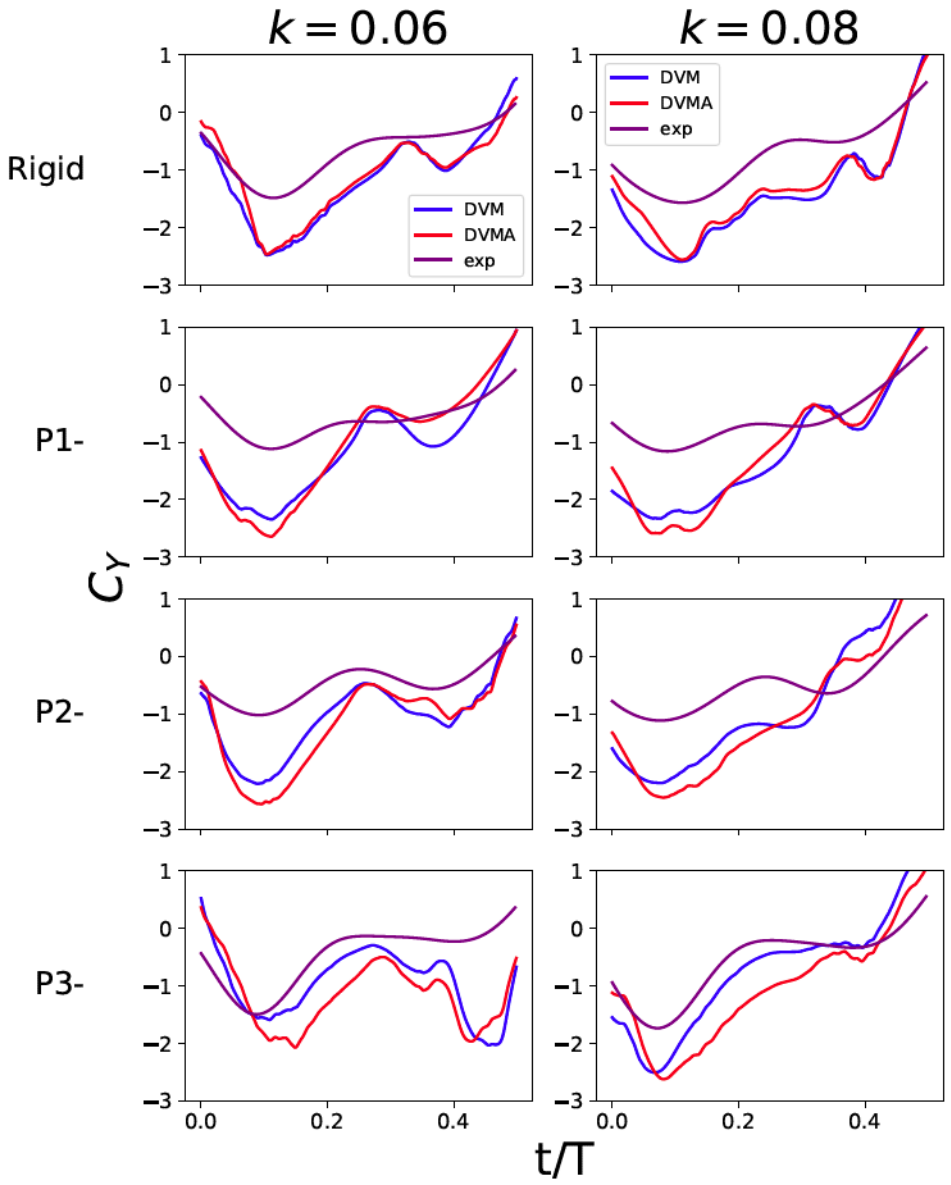

FIGURE 5.16: Comparison of lift force computed by the model, both with and without the empirical force correction, to the experimental data for the negative motions. DVM is the force predicted by the model without any empirical correction, DVMA is the force predicted by the model with the empirical force correction, and exp is the force measured from the experiment. The left and right columns are $k = 0.06$ and 0.08 respectively. The rows correspond to the rigid case, P1-, P2-, and P3- respectively.

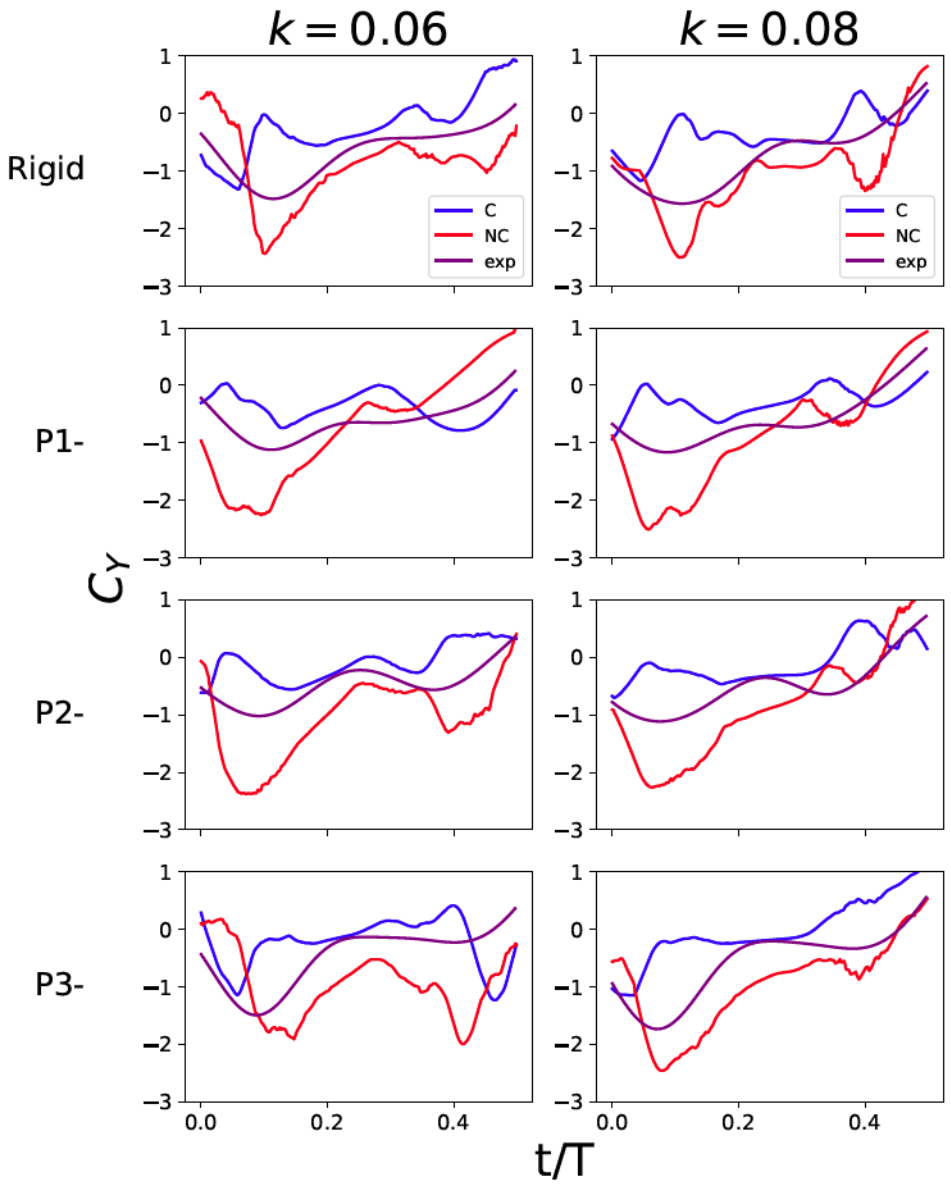

FIGURE 5.17: Comparison of the circulatory and non-circulatory forces from the model for the negative motions. C is the circulatory and NC is the non-circulatory. The total experimental lift force, exp, is also shown. The left and right columns are $k = 0.06$ and 0.08 respectively. The rows correspond to the rigid case, P1-, P2-, and P3- respectively.

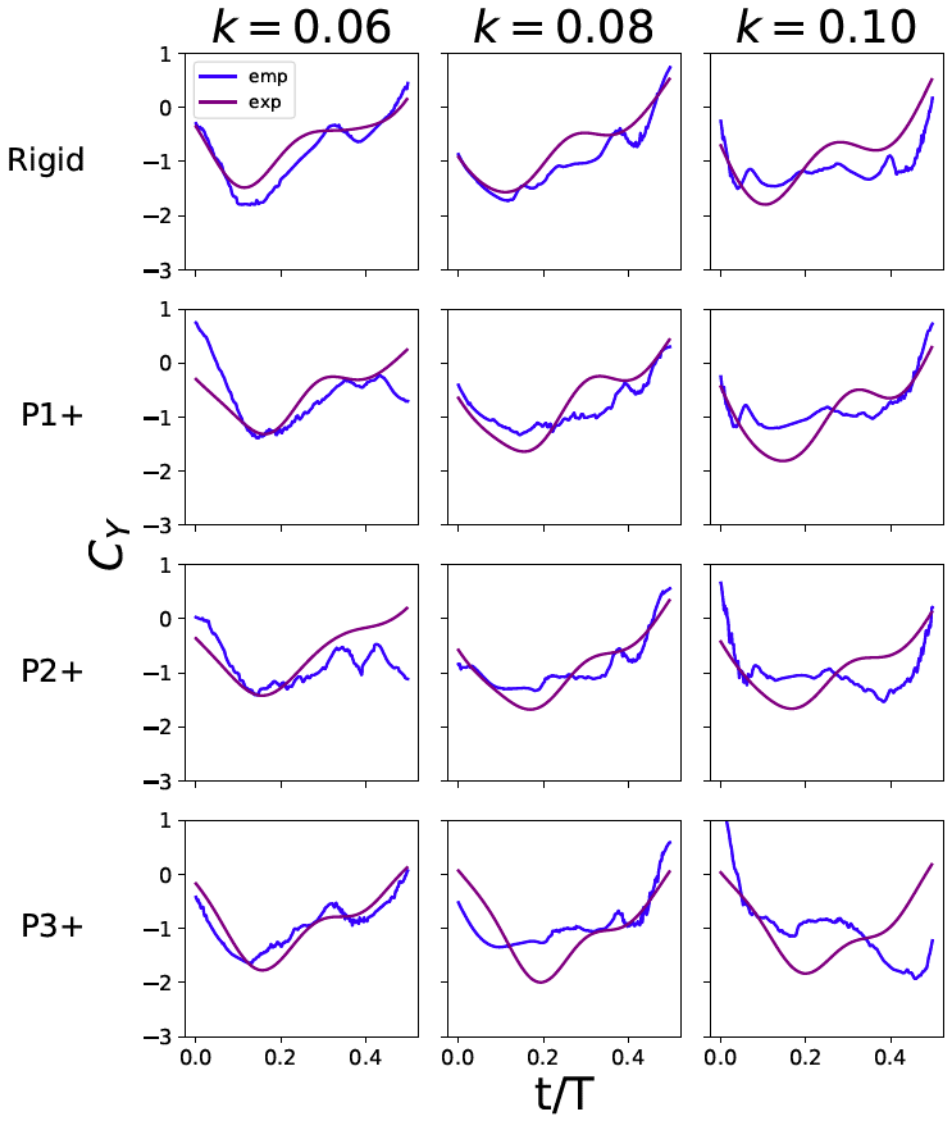

FIGURE 5.18: Comparison between force predicted by model with the adjustment given by Eqn 5.2 ("Emp") and the experimental forces ("Exp") for the positive motions.

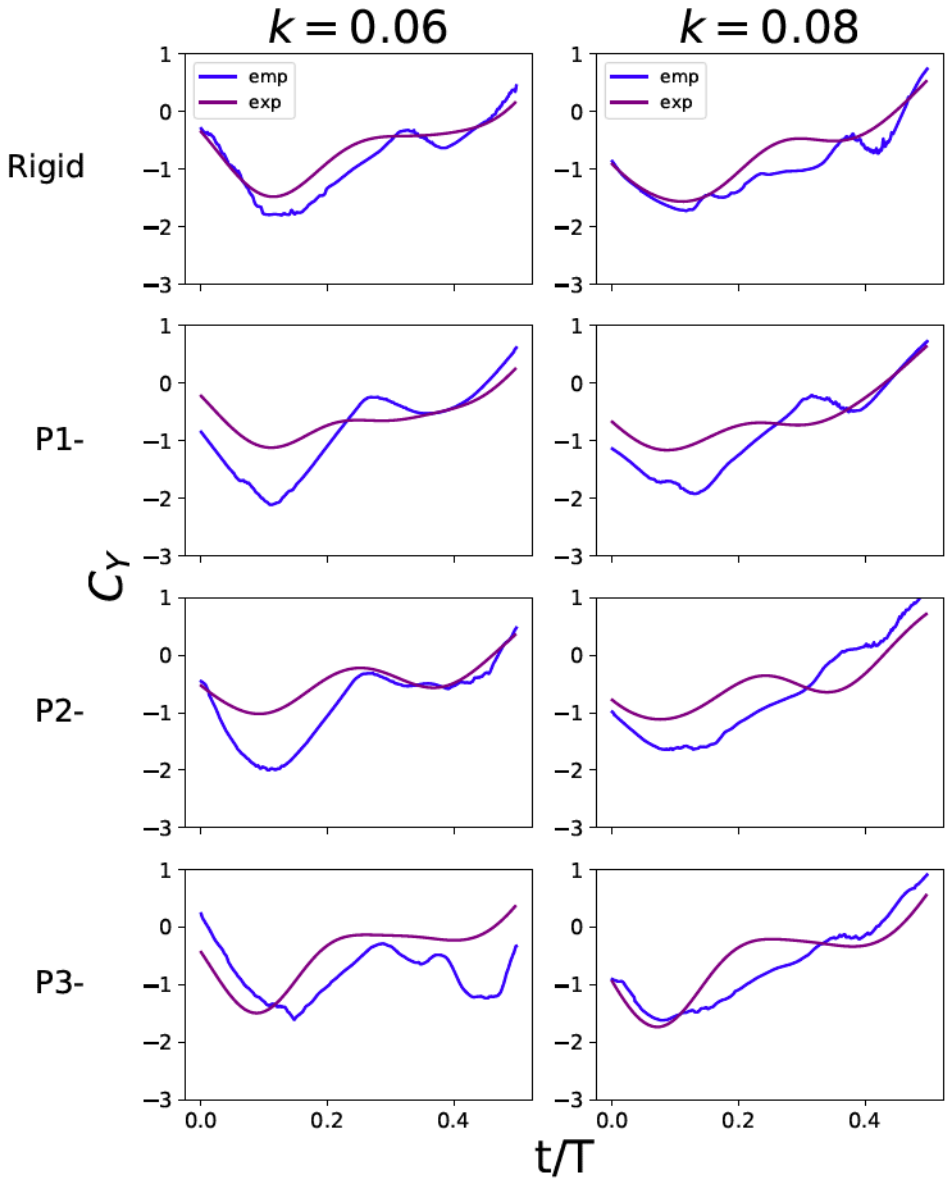

FIGURE 5.19: Comparison between force predicted by model with the adjustment given by Eqn 5.2 ("Emp") and the experimental forces ("Exp") for the negative motions.

The model follows the experiments well for positive motions at $k = 0.06$. For P1+ at $k = 0.06$ the model starts at $C_Y = 0.6$ at $t/T = 0$ but quickly decreases to $C_Y = -1.3$ at $t/T = 0.15$ and increases up to $C_Y = -0.5$ at $t/T = 0.35$ which compares well with the experiments. For P2+ the model deviates from the experiment at $t/T = 0.4$ with $C_Y = -1.1$ compared to the experimental value of $C_Y = -0.3$. For P3+ the model predicts the primary peak slightly earlier then the experiment.

At $k = 0.08$ and 0.10 the model under predicts the force magnitudes during the primary peak and over predicts the forces later during the stroke. At $t/T = 0.15$ for P1+ at $k = 0.08$ the model shows $C_Y = -1.2$ where as the experiment shows $C_Y = -1.5$; later in the stroke at $t/T = 0.3$ the model has $C_Y = -1$ where as the experiment has $C_Y = -0.3$. The model forces for P3+ at $k = 0.10$ are skewed later in the stroke with the primary peak occurring at $t/T = 0.45$ with a value of $C_Y = -2$.

The model results with the modified empirical correction for the negative motions are shown in Figure 5.19. for P1- and P2- at $k = 0.06$ the model shows $C_Y = -2$ at $t/T = 0.1$ where as the experiment shows $C_Y = -1$. Later in the stroke at $t/T = 0.4$ the model predicts the force better with $C_Y = -0.75$. For P3- at $k = 0.06$ the model predicts the correct primary peak value of $C_Y = -1.5$ but shows it occuring later at $t/T = 0.15$ where as the experiment shows it at $t/T = 0.09$. Later in the stroke at $t/T = 0.3$ the model predicts $C_Y = -0.75$ where as the experiment shows $C_Y = -0.4$; at $t/T = 0.45$ the model has $C_Y = -1.6$ where as the experiment has $C_Y = -0.4$.

For $k = 0.08$ the model does not capture the shape of the force curves as well. For P2- the shape of the forces predicted by the model are roughly quadratic where as the forces from the experiment have a secondary peak later in the stroke. For P3- the model correctly predicts the forces from $t/T = 0 - 0.1$ but does not capture the loss of lift between $t/T = 0.15 - 0.3$.

6 Discussion

The experimental data for the rigid cases show improving heaving efficiency with increasing reduced frequency. The force curves for $k = 0.06$ and 0.08 are indistinguishable with a large primary peak early in the stroke and a saddle later in the stroke. At the highest reduced frequency of $k = 0.10$ a secondary peak is present later in the stroke and the forces at this time are larger. Increasing reduced frequency decreases effective angle of attack and more lift is retained later in the stroke.

P2+ and P3+ motions have increased heaving power coefficients and efficiency compared to the rigid case. For $k = 0.06$ and 0.08, both P2+ and P3+ shift the primary peak lift coefficient later in the stroke compared to the rigid case. P3+ shows the largest primary peak value compared to all other motions. Shifting the primary peak later in the stroke is beneficial for energy harvesting since the peak force occurs during a higher heaving velocity. For $k = 0.10$ the primary peak lift coefficient values for the positive motions are comparable to the rigid case, but the primary peaks are still shifted later in the stroke. P2+ and P3+ have larger forces later in the stroke compared to the rigid case across all reduced frequencies.

The negative motions show decreased heaving power coefficients and efficiency compared to the rigid case. Both P1- and P2- have reduced primary peaks compared to the rigid case for both $k = 0.06$ and 0.08. For P3- the primary peak is comparable to the rigid case, but the lift decreases to close to zero later in the stroke.

All the positive motions have smaller effective angle of attack compared to the rigid case up to $t/T = 0.1$ and P3+ has smaller rate of change of effective angle of attack early in the stroke. P3+ has the smallest effective angle of attack amplitude of any motion. The negative motions all have larger effective angles of attack compared to the rigid case up to $t/T = 0.2$ and P3- has the largest rate of change of effective angle of attack as well as the largest effective angle of attack amplitude.

The energy harvesting performance is dependent on effective angle of attack. For this parameter range, both smaller effective angle of attack early in the stroke and decreased rate of change of effective angle of attack cause the primary peak to shift later in the stroke; P1+ and P2+ have reduced $|\alpha_{eff}|$ compared to the rigid case early in the stroke, and P3+ has both reduced $|\alpha_{eff}|$ and reduced rate of change of α_{eff}. This causes the

primary peaks to shift later in the stroke compared to the rigid case. P1- and P2- have large effective angle of attack magnitudes early in the stroke and have reduced primary peak force values. P3- has large effective angle of attack magnitudes early in the stroke and also has a high rate of change of effective angle of attack; P3- has very small forces later in the stroke and it is speculated that this is due to stall from large effective angle of attack.

The maximum effective angle of attack experienced during the cycle is not enough to predict the performance of the foil; the history of α_{eff}, when it is large and small during the stroke, is essential in determining the performance. This was illustrated in Figure 5.9 where the efficiency was plotted against the time averaged feathering parameter χ^* which includes information on the leading edge motion. The data collapses roughly linearly in this parameter space.

The model assumes that for fixed airfoil geometry and Reynold's number there is a single critical LESP value which determines the maximum suction that the airfoil leading edge can sustain [1]. The critical LESP values for the rigid cases are close with $LESP_{crit} = 0.08, 0.13, 0.11$ for $k = 0.06$, 0.08, and 0.10. The critical LESP values for both the positive and negative motions fluctuate; there is no strong relationship between the critical LESP value and the reduced frequency or the leading edge motion. The vortex shedding mechanism implemented here is not consistent and is ill suited for this parameter space.

Using the appropriate critical LESP values the model is moderately successful at predicting generic trends but largely fails to give accurate quantitative values. The model consistently over estimates the forces sometimes by 100%. In this low reduced frequency range vortices are shed from the leading edge frequently and this process contributes significantly to the lift force via the non-circulatory component. As vorticity is shed from the foil at the leading edge the non-circulatory force increases and the circulatory force decreases. The non-circulatory force is largely responsible for the primary peak in force as well as the secondary peak that the model predicts later in the stroke.

Applying an empirical correction only to the circulatory and suction components is inadequate; a correction should also be applied to the non-circulatory component. Doing so improves the model comparison to the experiments for some of the motions. While this modified force evaluation improves the model predictions, at higher reduced frequencies the primary peak is under predicted and the forces later in the stroke are over predicted. The model is unable to predict key trends from the experiments; it does not predict how

the primary peak shifts later in the stroke or the larger forces later in the stroke as seen in the experiments for the positive motions.

7 Conclusion

The effect of relative motion at the leading edge of a flapping foil energy harvester in the low reduced frequency range was studied using force measurements and a low order discrete vortex model was implemented. It was found that leading edge motion profiles in which the leading edge is rotated so as to reduce the effective angle of attack can improve the heaving efficiency of the airfoil. Both reducing the effective angle of attack early in the stroke and reducing the rate of change of effective angle of attack cause the primary force peak to shift later in the stroke. Leading edge motions that increase the effective angle of attack early in the stroke decrease the energy harvesting performance. Large effective angles of attack early in the stroke coupled with high rate of change of effective angle of attack cause loss of the lift later in the stroke.

The dicrete vortex model with vortex shedding at the leading edge based on the LESP is able to predict generic trends but unable to reproduce accurate quantitative values. Critical LESP values for the rigid cases across the reduced frequencies are similar. The critical LESP value for almost all motions fall between $LESP_{crit} = 0 - 0.2$. There is no clear relationship between the critical LESP value and the reduced frequency or leading edge motion; the vortex shedding mechanism is not consistent in this parameter space. A trailing edge separation correction based on Beddos [36] is inadequate because it only modifies the force from the bound circulation and here a significant portion of the force is generated by the vortex shedding process. Applying empirical corrections to the non-circulatory forces as well modestly improves the results.

While this work focused on reduced frequencies below the optimal range, the results here are still of interest and could be applied to real world energy harvesters. The optimal reduced frequency range is generally regarded as $fc/U_\infty = 0.12 - 0.18$ and a real world setup would be designed to fall within that range. However, during above average wind speeds the foil operation may fall below this reduced frequency range thus decreasing the performance of the foil. An active control setup such as the one investigated here could be used to increase the performance during these off peak scenarios.

Future work should investigate whether these trends extend into the moderate to high reduced frequency range. The power needed to implement the leading edge motion is currently unknown and would affect the overall performance of the energy harvester.

Flow visualization, such as PIV, would reveal how exactly the unsteady flow is affected by the leading edge motions implemented here. For low order modeling, future efforts should focus on more robust methods for shedding vorticity at the leading and trailing edge in these low reduced frequency ranges where the Kutta condition is violated so as to better reproduce the vorticity distribution in the flow field.

A An Appendix

A.1 Bernoulli Evaluation

From Katz and Plotkin in tangential and normal coordinates [31]:

$$\frac{P_\infty - P}{\rho} = \frac{1}{2}\left((\frac{\partial \Phi}{\partial s})^2 + (\frac{\partial \Phi}{\partial n})^2\right) - (\vec{U}_\infty + \dot{\vec{\theta}}_p \times \vec{r}) \cdot \nabla \Phi + \frac{\partial \Phi}{\partial t} \tag{A.1}$$

To evaluate the last term in Eqn A.1

$$\nabla \Phi = \vec{q} \tag{A.2}$$

$$\nabla \Phi \cdot d\vec{s} = d\Phi \tag{A.3}$$

$$d\Phi = q_s ds + q_n dn \tag{A.4}$$

Now integrate in the tangential direction, s, and the normal direction, n, where the integration over n is infinitesimal from one side of the panel to the other.

$$\Phi = \int_{LE}^{s} q_s ds + \int_{n-}^{n+} q_n dn \tag{A.5}$$

$$\int_{n-}^{n+} q_n dn = 0 \tag{A.6}$$

$$\Phi = \int_{LE}^{s} q_s ds = \int_{LE}^{s} \frac{\partial \Phi_b}{\partial s} + \frac{\partial \Phi_{shed}}{\partial s} ds \tag{A.7}$$

where ϕ_b and ϕ_{shed} are the velocity potentials from the bound vorticity and shed vortices respectively. LE denotes the leading edge.

$$\frac{d\Phi}{dt} = \frac{d}{dt}\int_{LE}^{s} q_s ds = \frac{d}{dt}\int_{LE}^{s} \frac{\partial \Phi_b}{\partial s} + \frac{\partial \Phi_{shed}}{\partial s} ds \tag{A.8}$$

$$\frac{P_\infty - P}{\rho} = \frac{1}{2}\left(\frac{\partial}{\partial s}\left(\Phi_b + \Phi_{shed}\right)^2 + \frac{\partial}{\partial n}\left(\Phi_b + \Phi_{shed}\right)^2\right) - (\vec{U}_\infty + \dot{\vec{\theta}}_p \times \vec{r}) \cdot \nabla(\Phi_b + \Phi_{shed}) + \frac{\partial}{\partial t}(\Phi) \tag{A.9}$$

From Katz and Plotkin [31] the velocity in the tangential direction on the top and bottom of a clockwise vorticity distribution is

$$\frac{\partial \Phi_{b,u}}{\partial s} = \Gamma(s)/2 \tag{A.10}$$

$$\frac{\partial \Phi_{b,l}}{\partial s} = -\Gamma(s)/2 \tag{A.11}$$

where u and l denote upper panel side and lower panel side. Subtract the pressure on the top surface from the bottom surface and simplify to get A.12

$$\frac{P_l - P_u}{\rho} = \Gamma(s)\left(\frac{\partial \Phi_{shed}}{\partial s} - (\vec{U}_\infty + \dot{\vec{\theta}}_p \times \vec{r})_s\right) + \frac{\partial \Phi_{b,u}}{\partial t} - \frac{\partial \Phi_{b,l}}{\partial t} \tag{A.12}$$

$$\frac{P_l - P_u}{\rho} = \Gamma(s)\left(\frac{\partial \Phi_{shed}}{\partial s} - (\vec{U}_\infty + \dot{\vec{\theta}}_p \times \vec{r})_s\right) + \frac{\partial}{\partial t}\int_{LE}^{s} \Gamma(s) ds \tag{A.13}$$

When vortex shedding occurs at the leading edge the line of integration must go past the leading edge around the most recently shed vortex. Therefore the change in vorticity of the most recently shed vortex contributes to the unsteady term in A.13.

A.2 Bernoulli and Impulse Comparison

The force evaluation using Bernoulli's equation and the vortex impulse method are compared for $k = 0.10$ rigid case in Figure A.1 and the circulatory and non-circulatory components are shown. The non-circulatory components match nearly perfectly. There is a small deviation between the circulatory components from each evaluation during

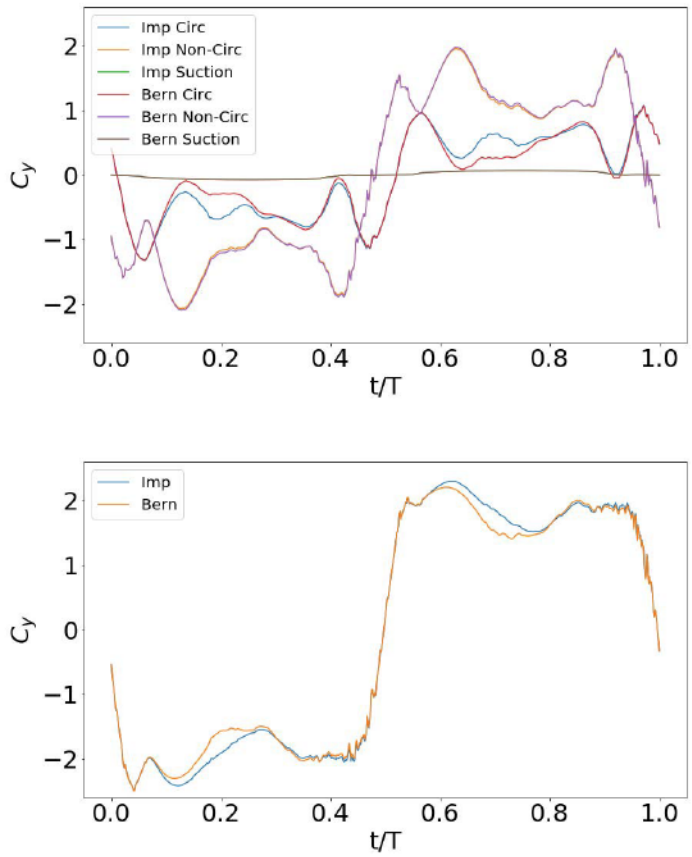

FIGURE A.1: Comparison of Bernoulli and vortex impulse force evaluations for $k = 0.10$ rigid case. 'Bern':Bernoulli. 'Imp':Impulse, 'circ':circulatory, 'non-circ':non-circulatory.

the mid stroke. The suction force is very small. All model results shown in this work were calculated using Bernoulli's equation.

A.3 Comparison of Experimental Forces With and Without the Motor Present

The measured lift force with the motor installed at the leading edge and without the motor installed at the leading edge is shown in Figure A.2. The two force curves follow each other very closely; there is some deviation at the primary peak for the upstroke but both curves are within each others' uncertainty.

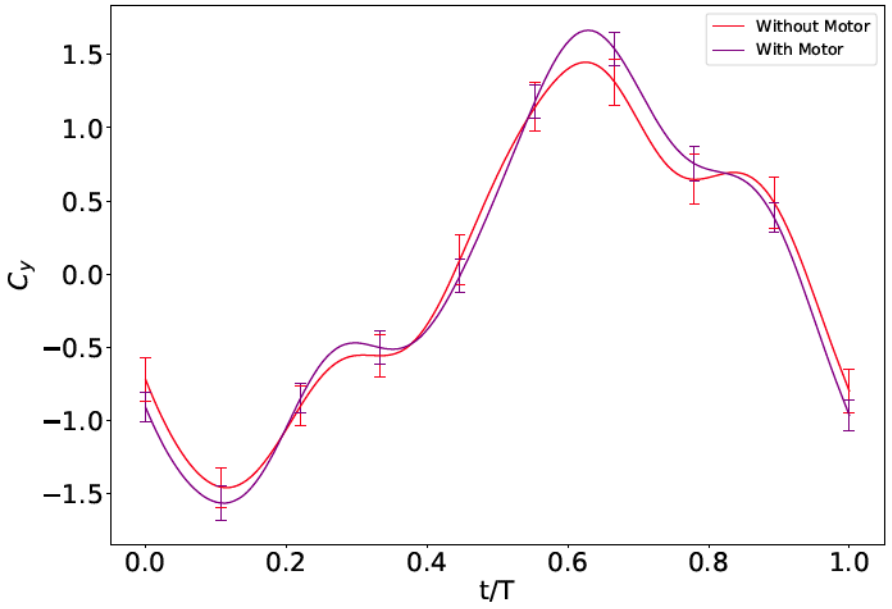

FIGURE A.2: Comparison of the measured lift coefficient with and without the motor installed at the leading edge.

A.4 Data Reduction Example

In Figure A.4 an example of the force data from the 1st min and 3rd min of data collection for $k = 0.08$ rigid case are shown; the forces are transferred to the mid span using Eqn 4.2. The force data for the first minute is purely inertial forces. The force data for the third minute is composed of both inertial forces and aerodynamic forces of interest. The force curves are subtracted and the results are scaled using Eqn 2.6 to get the lift coefficient. The calculated lift coefficient for all data sets for this set point are shown.

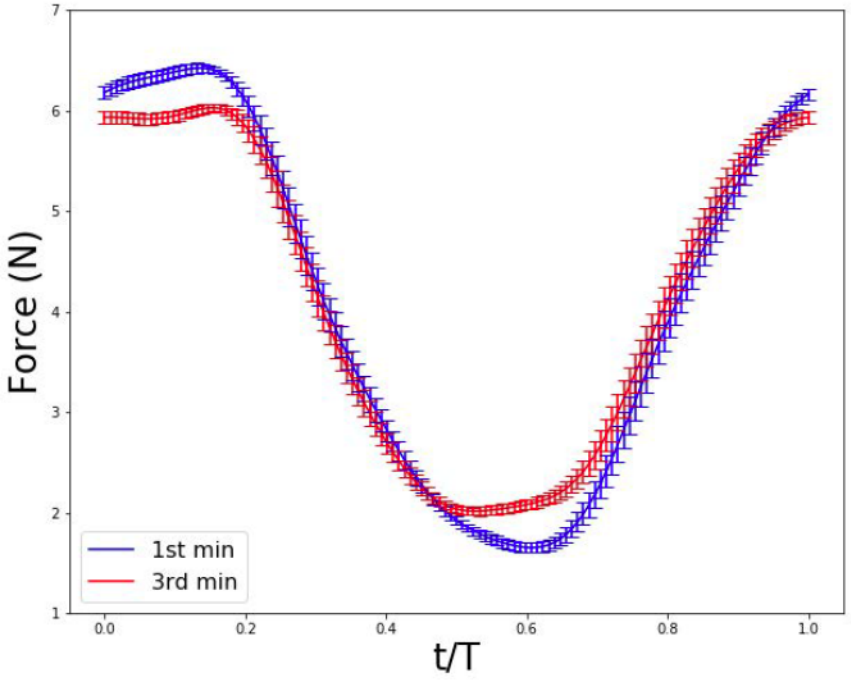

FIGURE A.3: Example of force distributions of the 1st minute, corresponding to the inertial forces, and the 3rd minute corresponding to the inertial and aerodynamic forces for $k = 0.08$ rigid. All forces are moved to the center span of the foil via Eqn 4.2. Error bars denote two standard deviations over the cycle averaging process.

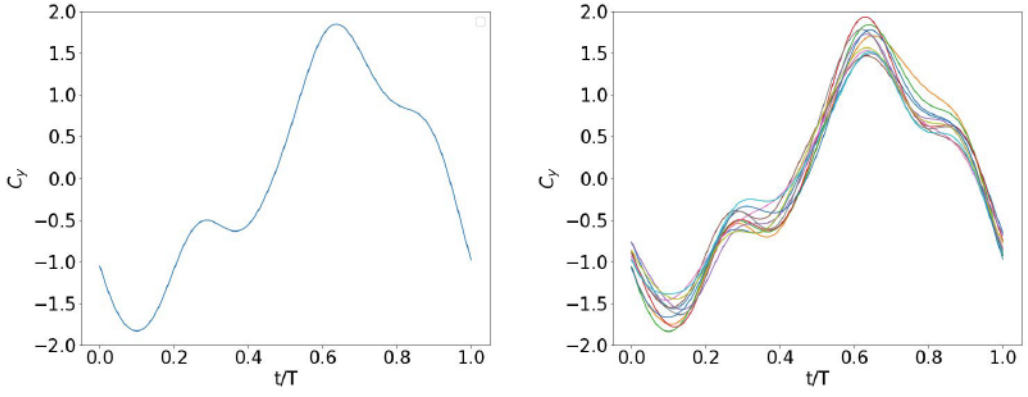

(a) (b)

FIGURE A.4: Example of data reduction for $k = 0.08$ rigid. (a) Lift Coefficient calculated by subtracting the forces from the 1st minute from the 3rd minute. (b) Lift coefficients from all data sets for the set point.

Bibliography

[1] Kiran Ramesh, Ashok Gopalarathnam, Kenneth Granlund, Michael Ol, and Jack Edwards. Discrete-vortex method with novel shedding criterion for unsteady aerofoil flows with intermittent leading-edge vortex shedding. *Journal of Fluid Mechanics*, 751:500–538, 2014.

[2] Thomas Kinsey and Guy Dumas. Parametric study of an oscillating airfoil in a power-extraction regime. *American Institute of Aeronautics and Astronautics Journal*, 46:1318–1330, 2008.

[3] Yeon Baik, Luis Bernal, Kenneth Granlund, and Michael Ol. Unsteady force generation and vortex dynamics of pitching and plunging aerofoils. *Journal of Fluid Mechanics*, 709:37–68, 2012. ISSN 00221120. URL http://search.proquest.com/docview/1095109614/.

[4] Qiang Zhu. Optimal frequency for flow energy harvesting of a flapping foil. *Journal of Fluid Mechanics*, 675:495–517, 2011.

[5] Meilin Yu and Z Wang. Numerical simulation of oscillating-wing based energy harvest mechanism using the high-order spectral difference method. *31st AIAA Applied Aerodynamics Conference*, 06 2013. doi: 10.2514/6.2013-2670.

[6] Jean-Christophe Veilleux and Guy Dumas. Numerical optimization of a fully-passive flapping-airfoil turbine. *Journal of Fluids and Structures*, 70:102130, 04 2017. doi: 10.1016/j.jfluidstructs.2017.01.019.

[7] Alexander D. Totpal, Firas F. Siala, and James A. Liburdy. Energy harvesting of an oscillating foil at low reduced frequencies with rigid and passively deforming leading edge. *Journal of Fluids and Structures*, 82:329–342, 2018. ISSN 0889-9746.

[8] Firas Siala, Michael W. Prier, and James Liburdy. Force production mechanisms of a heaving and pitching foil operating in the energy harvesting regime. page V001T07A002, 07 2018. doi: 10.1115/FEDSM2018-83111.

[9] Daegyoum Kim, Benjamin Strom, Shreyas Mandre, and Kenneth Breuer. Energy harvesting performance and flow structure of an oscillating hydrofoil with finite span. *Journal of Fluids and Structures*, 70:314–326, 2017. ISSN 0889-9746.

[10] Alexander Widmann. *Formation and Detachment of Leading Edge Vortices on Unsteady Airfoils*. PhD thesis, Technische Universitt, 2015.

[11] William McKinney and James Delaurier. The wingmill: an oscillating-wing windmill. *Journal of Energy*, 5:109–109, 1981.

[12] Qing Xiao, Wei Liao, Shuchi Yang, and Yan Peng. How motion trajectory affects energy extraction performance of a biomimic energy generator with an oscillating foil? *Renewable Energy*, 37(1), 2011. ISSN 0960-1481.

[13] Lubao Teng, Jian Deng, Dingyi Pan, and Xueming Shao. Effects of non-sinusoidal pitching motion on energy extraction performance of a semi-active flapping foil. *Renewable Energy*, 85(C):810–818, 2016. ISSN 0960-1481.

[14] Yonghui Xie, Kun Lu, and Di Zhang. Investigation on energy extraction performance of an oscillating foil with modified flapping motion. *Renewable Energy*, 63 (1):550–557, 2014. ISSN 0960-1481.

[15] Firas Siala and James A. Liburdy. Energy harvesting of a heaving and forward pitching wing with a passively actuated trailing edge. *Journal of Fluids and Structures*, 57(C):1–14, 2015. ISSN 0889-9746.

[16] David Rival, Jochen Kriegseis, Pascal Schaub, Alexander Widmann, and Cameron Tropea. Characteristic length scales for vortex detachment on plunging profiles with varying leading-edge geometry. *Experimental Fluids*, 55:1660, 2014.

[17] Wendi Liu, Qing Xiao, and Fai Cheng. Abio-inspired study on tidal energy extraction with flexible flapping wings. *Bioinspiration Biomimetics*, 8(3), 2013. ISSN 1748-3182.

[18] Fang-Bao Tian, John Young, and Joseph C.S. Lai. Improving power-extraction efficiency of a flapping plate: From passive deformation to active control. *Journal of Fluids and Structures*, 51:384–392, 2014. ISSN 0889-9746.

[19] C.M. Hoke, J. Young, and J.C.S. Lai. Effects of time-varying camber deformation on flapping foil propulsion and power extraction. 56:152–176, 2015. ISSN 0889-9746.

[20] Wendi Liu, Qing Xiao, and Qiang Zhu. Passive flexibility effect on oscillating foil energy harvester. *AIAA Journal*, 54(1):1172–1187, 2016. ISSN 0001-1452.

[21] Jie Wu, Chang Shu, N Zhao, and Fang-Bao Tian. Numerical study on the power extraction performance of a flapping foil with a flexible tail. *Physics of Fluids*, 27: 013602, 01 2015. doi: 10.1063/1.4905537.

[22] Zhengliang Liu, Fang-Bao Tian, John Young, and Joseph Lai. Flapping foil power generator performance enhanced with a spring-connected tail. *Physics of Fluids*, 29, 12 2017. doi: 10.1063/1.4998202.

[23] Bing Zhu, Yun Huang, and Yongming Zhang. Energy harvesting properties of a flapping wing with a adaptive gurney flap. *Energy*, 152:117–128, 06 2018.

[24] T Kinsey and G Dumas. Optimal operating parameters for an oscillating foil turbine at reynolds number 500,000. *AIAA Journal*, 52(9):1885–1895, 2014. ISSN 0001-1452.

[25] Jian Deng, C. P. Caulfield, and Xueming Shao. Effect of aspect ratio on the energy extraction efficiency of three-dimensional flapping foils. *Physics of Fluids*, 26(4), 2014. ISSN 1070-6631.

[26] Thomas Kinsey and Guy Dumas. Three-dimensional effects on an oscillating-foil hydrokinetic turbine.(author abstract)(report). *Journal of Fluids Engineering*, 134 (7), 2012. ISSN 0098-2202.

[27] T. Kinsey, G. Dumas, G. Lalande, J. Ruel, A. Mhut, P. Viarouge, J. Lemay, and Y. Jean. Prototype testing of a hydrokinetic turbine based on oscillating hydrofoils. *Renewable Energy*, 36(6):1710–1718, 2011. ISSN 0960-1481.

[28] Hunkee Cho and Qiang Zhu. Performance of a flapping foil flow energy harvester in shear flows. *Journal of Fluids and Structures*, 51:199–210, 2014. ISSN 0889-9746. URL http://search.proquest.com/docview/1654669533/.

[29] Jian Deng, Lubao Teng, Dingyi Pan, and Xueming Shao. Inertial effects of the semi-passive flapping foil on its energy extraction efficiency. *Physics of Fluids*, 27 (5), 2015. ISSN 1070-6631.

[30] Louie Milne-Thompson. *Theoretical Hydrodynamics*. Dover Publications Inc, 1968.

[31] Joseph Katz and Allen Plotkin. *Low-Speed Aerodynamics*. Cambridge University Press, 2001.

[32] J Katz. A discrete vortex method for the non-steady separated flow over an airfoil. *Journal of Fluid Mechanics*, 102:315–328, 1981. ISSN 0022-1120. URL http://search.proquest.com/docview/23639526/.

[33] S A Ansari, R bikowski, and K Knowles. Non-linear unsteady aerodynamic model for insect-like flapping wings in the hover. part 2: Implementation and validation. *Proceedings of the Institution of Mechanical Engineers, Part G: Journal of Aerospace Engineering*, 220(3):169–186, 2006. ISSN 0954-4100.

[34] Kiran Ramesh, Ashok Gopalarathnam, Jack Edwards, Michael Ol, and Kenneth Granlund. An unsteady airfoil theory applied to pitching motions validated against experiment and computation. *Theoretical and Computational Fluid Dynamics*, 27 (6):843–864, November 2013. ISSN 0935-4964.

[35] Zhengliang Liu, Joseph C. S. Lai, John Young, and Fang-Bao Tian. Discrete vortex method with flow separation corrections for flapping-foil power generators.(author abstract). *AIAA Journal*, 55(2), 2017. ISSN 0001-1452.

[36] T. S. Beddoes. A semi8208;empirical model for dynamic stall. *Journal of the American Helicopter Society*, 34(3):3–17, 1989. ISSN 2161-6027.

[37] Chengjie Wang and Jeff Eldredge. Low-order phenomenological modeling of leading-edge vortex formation. *Theoretical and Computational Fluid Dynamics*, 27(5):577–598, 2013. ISSN 0935-4964.

[38] Fo Minotti. Unsteady two-dimensional theory of a flapping wing. *Physical Review E*, 66(5), 2002. ISSN 1539-3755.

[39] X. Xia and K. Mohseni. Lift evaluation of a two-dimensional pitching flat plate. *Physics of Fluids*, 25(9), 2013. ISSN 1070-6631.

[40] G. Vatistas, V. Kozel, and W. Mih. A simpler model for concentrated vortices. *Experiments in Fluids*, 11(1):73–76, 1991. ISSN 0723-4864.

[41] A Leonard. Vortex methods for flow simulation. *Journal of Computational Physics*, 37:289–335, 1980. ISSN 0021-9991. URL http://search.proquest.com/docview/23935914/.

[42] J Li and Zn Wu. Unsteady lift for the wagner problem in the presence of additional leading/trailing edge vortices. *Journal Of Fluid Mechanics*, 769:182–217, 2015. ISSN 0022-1120.

[43] Chenyuan Bai, Juan Li, and Ziniu Wu. Generalized kuttajoukowski theorem for multi-vortex and multi-airfoil flow with vortex production a general model. *Chinese Journal of Aeronautics*, 27(5):1037–1050, 2014. ISSN 1000-9361.

[44] Kiran Ramesh, Kenneth Granlund, Michael Ol, Ashok Gopalarathnam, and Jack Edwards. Leading-edge flow criticality as a governing factor in leading-edge vortex initiation in unsteady flows. *Theoretical and Computational Fluid Dynamics*, 2017.

[45] Yigyang Fan. *Identification of an Unsteady Aerodynamic Model up to High Angle of Attack Regime*. PhD thesis, Virginia Tech, 1997.

[46] Alex Totpal. The Energy Extraction Performance of an Oscillating Rigid and Flexible Foil. Master's thesis, Oregon State University, Corvallis, Oregon, 2017.